MODELING TIME-RESOLVED INTERACTION FORCE MODE AFM IMAGING

A Thesis
Presented to
The Academic Faculty

by

Hasan Giray Oral

In Partial Fulfillment
of the Requirements for the Degree
Master of Science Mechanical Engineering in the
School of Mechanical Engineering

Georgia Institute of Technology
May 2012

Copyright © Hasan Giray Oral 2012

MODELING TIME-RESOLVED INTERACTION FORCE MODE AFM IMAGING

Approved by:

Dr. F. Levent Degertekin, Advisor
School of Mechanical Engineering
Georgia Institute of Technology

Dr. Peter J. Hesketh
School of Mechanical Engineering
Georgia Institute of Technology

Dr. Todd Sulchek
School of Mechanical Engineering
Georgia Institute of Technology

Date Approved: March 27th, 2012

To My Parents,

Gülşen and Mustafa Oral

ACKNOWLEDGEMENTS

It is a pleasure to express my most sincere thanks to everyone who contributed to this thesis. First and foremost, I would like to voice my deepest gratitude for my advisor, Dr. Levent Degertekin, who relentlessly supported and guided me throughout this invaluable experience. I would also like to thank Dr. Peter J. Hesketh, and Dr. Todd Sulchek for serving in my thesis committee and providing very helpful feedback to improve this thesis. I would also like to acknowledge my colleagues from the MIST group. Particularly, I feel indebted to Zehra Parlak and Hamdi Torun for training me in AFM and for their selfless efforts to help me progress. I would also like to thank Rameen Hadizadeh for fabricating FIRAT probes and Sarp Satir for his valuable help with technical matters.

I am grateful to all my friends in Atlanta for their company. Thanks to them, Atlanta is a second home. I cannot thank my parents enough for their love, support, and patience. This thesis is dedicated to them.

TABLE OF CONTENTS

ACKNOWLEDGEMENTS ... IV

LIST OF TABLES ... VII

LIST OF FIGURES ... VIII

SUMMARY ... XII

CHAPTER

1 INTRODUCTION AND BACKGROUND ... 1

1.1 Atomic Force Microscope ... 1

1.2 Material Characterization at Nanoscale by Atomic Force Microscopy ... 3

1.2.1 Methods ... 3

1.2.2 Limitations ... 9

1.3 Research Goals ... 12

2 FORCE SENSING INTEGRATED READOUT AND ACTIVE TIP PROBE ... 13

2.1 Imaging Modes and Applications of FIRAT Probe ... 15

2.1.1 Simultaneous Topography and Material Property Imaging by TRIF Mode AFM ... 15

2.1.2 Fast Tapping Mode Imaging ... 17

2.1.3 Combined Quantitative Ultrasonic and TRIF AFM Imaging ... 18

2.1.4 Active Tip Control ... 20

2.2 Summarizing Remarks ... 21

3 MODELING TIME-RESOLVED INTERACTION FORCE MODE IMAGING ... 22

3.1 FIRAT Probe Dynamics ... 23

3.2 Tip-Sample Interaction Model ... 26

3.2.1 Contact Mechanics Models ... 26

3.2.1.1 Hertzian Contact Model ... 27

3.2.1.2 Derjaguin-Muller-Toporov (DMT) Contact Model................ 27

3.2.1.3 Burnham-Colton-Pollock (BCP) Contact Model.................... 28

3.2.1.4 Johnson-Kendall-Roberts-Sperling (JKRS) Contact Model... 28

3.2.2 Comparison of Contact Mechanics Models.. 29

3.2.3 The Interaction Model via Contact and Non-contact Forces................ 30

3.3 Experimental Characterization of the Atomic Force Microscope Piezoactuator.. 31

3.4 Combined Simulink Implementation of the Imaging Model................................ 33

4 SIMULATION RESULTS AND EXPERIMENTAL VERIFICATION...................... 36

4.1 Effect of Elasticity Variations on Accurate Topography Measurement of Samples 36

4.2 Verification of the Imaging Model 38

4.3 Effect of Adhesion Variations on Accurate Topography Measurement of Samples 39

4.4 Simulation of Passive and Active Tip Control Schemes 41

4.4.1 Simulation of Topography Measurement by ATC 43

4.4.2 Experiment.. 46

5 CONCLUSION.. 48

5.1 Future Work 48

APPENDIX

A ANALOG ATC CIRCUITRY FOR TRIF MODE AFM IMAGING........................... 51

A.1 ATC Circuitry 51

B FPGA IMPLEMENTATION OF ATC AND PEAK FORCE BASED PID CONTROL 55

B.1 FPGA Program.. 55

B.2 Comments.. 59

REFERENCES 61

LIST OF TABLES

Page

Table 4.1: FIRAT Probe Properties and Imaging Parameters Used in Simulations 36

LIST OF FIGURES

Page

Figure 1.1: Left: Atomic Force Microscope (AFM). Right: AFM cantilever probe. 1

Figure 1.2: AFM imaging modes: a) Non-contact mode. b) Contact mode c) Intermittent contact mode. 2

Figure 1.3: Force-distance curve measured with an AFM cantilever probe. The cantilever approaches the surface (1), jumps into contact under the effect of attractive forces (2), indents the sample surface as the repulsive forces dominate the interaction (3), starts receding from contact (4), undergoes adhesive forces before losing contact with the sample (5), moves away from the sample surface (6). 4

Figure 1.4: a) Harmonic cantilever with a rectangular opening. b) As the cantilever is excited at its fundamental resonance (37.4 kHz), the 6th (240 kHz) and 16th (598 kHz) harmonics are enhanced by the coinciding cantilever resonances. These harmonics are the means for imaging material properties [23]. 6

Figure 1.5: a) Torsional harmonic cantilever: Flexural vibrations are tracked for imaging topography while torsional vibrations carry interaction force information b) Flexural (blue) and torsional (orange) frequency response of the torsional harmonic cantilever: High bandwidth of torsional response enable reconstruction of interaction forces [24]. 7

Figure 1.6: a) Cantilever with integrated force sensor: High resonance frequency of the small cantilever enables resolving interaction forces. Displacement detection is made possible by diffraction grating fingers. b) Coupling of unwanted vibrations to the sensing cantilever and lack of damping causes ringing before and after contact [26]. 8

Figure 1.7: Schematic of the atomic force acoustic microscopy (AFAM) setup. 8

Figure 1.8: a) Time-resolved interaction force signal when a cantilever with a stiffness of 65 N/m, resonance frequency of 282 kHz, and a Q factor of 522 is modulated at 2 kHz under peak force control. Ringing exceeds peak force value. b) The desired tip-sample interaction signal during simultaneous topography and material property imaging: Repulsive force is minimized while contact time is kept constant and ringing is eliminated. 11

Figure 2.1: Left: Schematic cross section of the FIRAT probe for AFM studies. Right: The scanning ion beam image of an actual FIRAT probe which will be used in this project [32]. 13

Figure 2.2: The change in photodetector output voltage as a function of the bias voltage applied between the diffraction gratings and the sensor membrane. The gap change due to applied bias alters the intensity of the first diffracted order [46]. 14

Figure 2.3: The FIRAT probe movement sequence and the resulting tip displacement signal during one cycle of contact with the sample. The z-piezo displacement that drives the FIRAT probe base is also given. As the tip approaches the sample, attractive forces pull the tip on the sample. The z-piezo extends until the desired force amplitude is reached, then retracts until the tip is pulled off the sample. The resulting photodiode output becomes the TRIF measurement [32]. 16

Figure 2.4: Experimental TRIFs measured by FIRAT probe on PEGDMA, PMMA, DEGDMA, and silicon samples. TRIFs contain sample elasticity and surface energy information that can be obtained using a suitable tip-sample interaction model [35]. 17

Figure 2.5: Tapping mode line scans of a periodic grating sample measured by FIRAT probe (a), and a cantilever probe (b). FIRAT probe is able to track the topography of the gratings at all scan rates, with some artifacts at 60 Hz. The cantilever fails to follow the steep edges at 5Hz, and the measurements do not reflect the actual topography of the sample at higher scan rates [32]. 18

Figure 2.6: Elasticity measurements on an aluminum-silicon-chromium sample by TRIF mode and combined UAFM and TRIF imaging. TRIF mode measurement shows larger standard deviation due to non-matching probe-sample stiffness at the TRIF mode frequency [37]. 19

Figure 2.7: a) FIRAT probe movement sequence and the corresponding TRIF signal during one interaction cycle. b) Once the repulsive force exceeds a user defined force threshold, an active control signal is generated. c) Active control signal is applied to the tip electrostatically so that it is pulled away from the sample without loss of contact and the repulsive force is limited at a desired value [36]. 20

Figure 3.1: Experimental setup of Time-resolved interaction force (TRIF) mode imaging, active tip control (ATC), and tapping mode AFM (TM AFM) operations using the FIRAT Probe. 23

Figure 3.2: Lumped Element Model of the FIRAT Probe. 24

Figure 3.3: Simulated frequency response of FIRAT Probe for different gaps. Damping of the probe increases due to squeezed-film effect, as the gap decreases. 25

Figure 3.4: Comparison of Hertz, DMT, BCP and JKRS contact mechanics models. 29

Figure 3.5: Simulated TRIF signal of FIRAT probe using the constructed interaction model. 30

Figure 3.6: Magnitude (top) and phase (bottom) response of the Multimode SPM piezoactuator as a function of frequency. The red asterisk represents the experimentally measured response. The blue solid line is the model fit to experimental data. 32

Figure 3.7: Simulink model of time-resolved interaction force (TRIF) imaging, active tip control (ATC), and tapping mode AFM (TM AFM) operations using active probes. 34

Figure 4.1: Simulated TRIF mode line scan of a soft step on a stiff surface. As the peak force is increased, the measured height of the step decreases due to indentation. 37

Figure 4.2: Simulated tapping mode line scan of a sample consisting of a 12 nm step with 2 GPa reduced elastic modulus over a flat surface with 100 GPa reduced elastic modulus. The simulated height of the step decreases as the peak tapping force increases. The height values agree well with simulation results in literature [21], which verifies the imaging model. 39

Figure 4.3: a) Simulated TRIF mode line scan of a step with constant elasticity but varying adhesion. Topography error due to adhesion can be eliminated by controlling the peak force value which is independent of adhesive forces. b) Interaction force signals during RMS control before (left), and after (right) the adhesion change. 40

Figure 4.4: Response of FIRAT probes with different bandwidth values to ATC. FIRAT probes become more responsive to ATC when the probe bandwidth is larger. 41

Figure 4.5: a) Contact time decreases for small repulsive forces during peak force control. The tip-sample contact becomes less stable and important material information such as elastic modulus and adhesion force is lost. b) Controlling repulsive forces with ATC provides sufficient contact time for stable contact and preserving material information. 43

Figure 4.6: a) AFM image of the test sample composed of silicon (E=150GPa) and polymer (E=2.8GPa). b) AFM image of the control sample composed of chromium (E=279GPa) and silicon (150GPa) [36]. 44

Figure 4.7: a) Simulated topography measurement of the test sample with and without ATC. ATC decreases the topography error of the polymer region by 2.26nm since repulsive forces on soft polymer are minimized. b) Simulated topography measurement of the control sample. The improvement is only 0.05nm since both chromium and silicon are stiff materials. 45

Figure 4.8: a) Measured topography of the test sample with (solid red line) and without (dashed blue line) ATC. The difference (dotted green line) between the two measurements is approximately 1nm on soft polymer, 0.3nm on stiff silicon, except for the spikes around the edges of topography. ATC improves topography measurement of the soft polymer region by minimizing the indentation. b) Measured topography of the control sample with (solid red line) and without (dashed blue line) ATC. The difference (dotted green line) is around 0.1nm on both silicon and chromium. Since the indentation into these stiff materials is already small, ATC improvement is negligible [36]. 47

Figure A.1: The ATC circuitry used in TRIF Mode AFM imaging. 52

Figure B.1: NI PXI 8176 real-time controller and NI PXI 7831R FPGA. 55

Figure B.2: Real-time controller program. Bottom portion (b) is the continuation of the top portion (a). 56

Figure B.3: Sections of the FPGA program for ATC (a), peak detection (b, c, d) and PID control (e). 57

Figure B.4: Graphical illustration of the peak detection algorithm. 58

SUMMARY

Intermittent contact mode atomic force microscopy has been widely employed for simultaneous topography imaging and material characterization. The work in the literature includes both qualitative and quantitative methods. Regular AFM cantilevers are generally used in these methods, yet these cantilevers come with certain limitations. These limitations result from the very nature of cantilever probes. They are passive force sensors with insufficient damping. This prevents having active and complete control on tip-sample forces, causing sample damage and inaccurate topography measurement. Ideally, an AFM probe should offer high bandwidth to resolve interaction forces, active control capability for small interaction force and stable operation, and sufficient damping to avoid transient ringing which causes undesired forces on the sample. Force sensing integrated readout and active tip (FIRAT) probe offers these properties. A special imaging mode, time-resolved interaction force (TRIF) mode imaging can be performed using FIRAT probe for simultaneous topography and material property imaging. The accuracy of topography measurement of samples with variations in elastic and adhesive properties is investigated via numerical simulations and experiments. Results indicate that employing FIRAT probe's active tip control (ATC) capability during TRIF mode imaging provides significant level of control over the tip-sample forces. This improves the accuracy of topography measurement during simultaneous material property imaging, compared to conventional methods. Moreover, Active tip control (ATC) preserves constant contact time during force control for stable contact while preventing loss of material property information such as elasticity and adhesive forces.

CHAPTER 1

INTRODUCTION AND BACKGROUND

1.1 Atomic Force Microscope

Due to its high imaging resolution, the atomic force microscope (AFM) has been an extremely useful tool for nanoscale characterization of materials since its invention [1]. It is possible to measure surface topography and material properties by AFM. Material properties that can be measured by AFM may include mechanical [7], electrical [2] and chemical [3] properties. Optical microscopy fails to provide high resolution due to the diffraction limit. While this diffraction limit is on the order of hundreds of nanometers, the AFM is capable of producing topography images of materials in subatomic resolution [4].

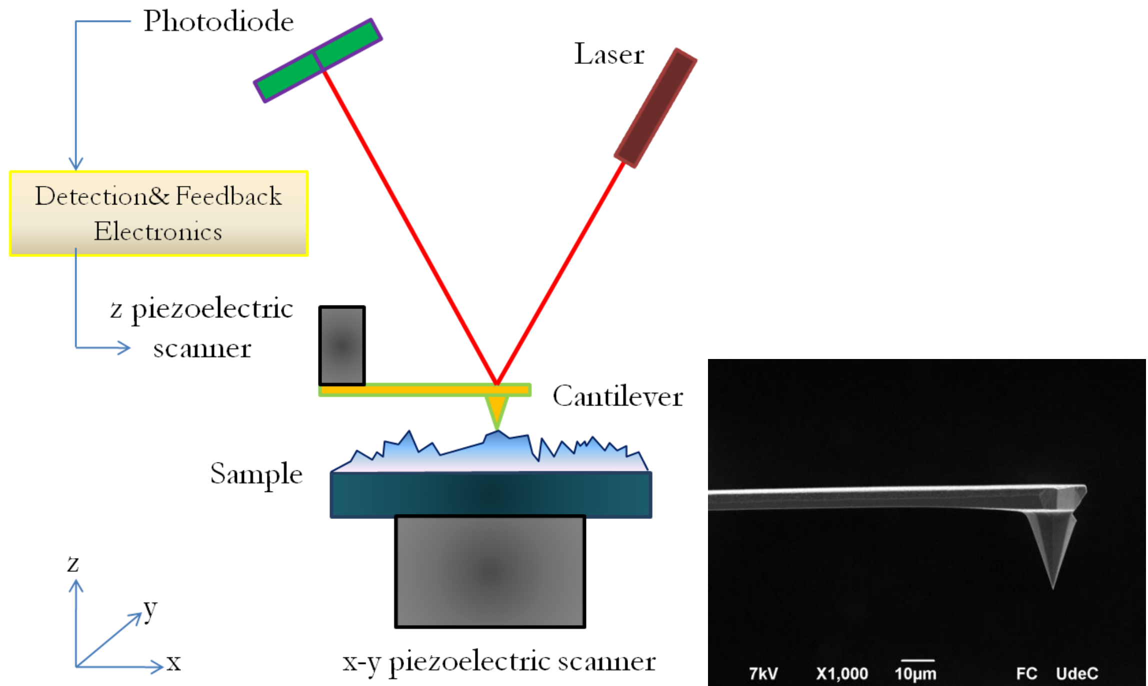

Figure 1.1 Left: Atomic Force Microscope (AFM). Right: AFM cantilever probe.

A conventional AFM is depicted in figure 1.1. The sensing structure is generally a micromachined cantilever probe with a sharp tip at the end. An SEM image of a cantilever probe is also shown in figure 1.1. The cantilever scans the sample surface by means of a piezoactuator. Piezoactuators are used in AFM systems for their accurate positioning capability in three dimensions at nanoscale. The interaction between the cantilever tip and the surface causes the cantilever to deflect. The deflection is most commonly detected by the optical lever method [5]. The laser beam that is reflected from the cantilever is captured by a photodiode. Detection and feedback electronics analyze the signal from the photodiode and maintain the scanning operation in closed loop. The conventional AFM system and the probe structure can be modified and redesigned in order to perform quantitative measurements or measure specific properties of materials. This is done throughout the literature, some of which are discussed in this thesis.

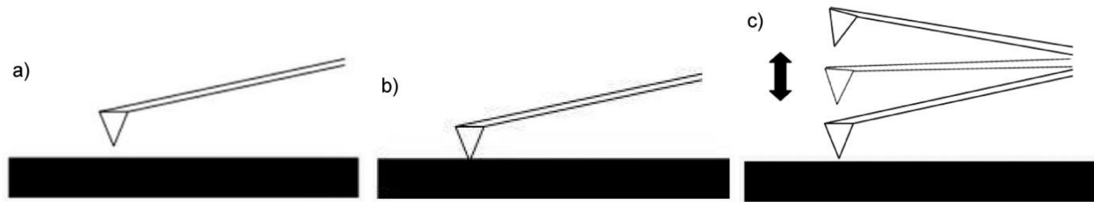

Figure 1.2 AFM imaging modes: a) Non-contact mode. b) Contact mode c) Intermittent contact mode.

There are mainly three operation modes in AFM. The modes are categorized according to the contact mechanism between the probe tip and the sample surface. These are non-contact (figure 1.2a), contact (figure 1.2b), and intermittent contact (figure 1.2c) modes. Non-contact mode utilizes the true atomic interactions between the probe tip and the sample surface. When the probe is brought closer to the sample, capillary and van der Waals forces attract the tip atoms towards the surface atoms. Due to variations in sample topography, the magnitude of attractive forces on the tip is not constant. Therefore, changes in cantilever deflection can be detected to measure topography. In contact mode, the tip is brought into contact with the sample and the interaction forces are repulsive. Due to shear (lateral) force that is present while scanning the surface, contact mode AFM

is not the preferred technique for imaging soft materials. In intermittent contact mode, the cantilever goes into and out of contact periodically, so it is under the effect of both attractive and repulsive forces. Shear forces are eliminated, therefore intermittent contact mode is less destructive to samples compared to contact mode. Intermittent contact mode is also preferable to non-contact mode in terms of stable tip-sample interaction. The most common type of intermittent contact mode techniques is the tapping mode [6]. In tapping mode, a resonant cantilever taps the surface while the change in the cantilever oscillation amplitude is tracked to measure the topography of the sample.

In addition to mapping topography, AFM can also be used to image material properties. The information for sample material properties is contained in the tip-sample interaction. Depending on the type of the interaction, the information may be related to mechanical, electrical or chemical properties of the sample. This thesis focuses on the mechanical aspect of the tip-sample interaction during intermittent contact mode AFM.

1.2 Material Characterization at Nanoscale by Atomic Force Microscopy

1.2.1 Methods

Tapping mode offers more than only measuring topography of materials. Phase imaging [7] employs conventional tapping mode technique while exploiting material information that is already contained in the tip-sample repulsive interactions. The phase angle of the cantilever's tapping oscillations depends on the magnitude of the repulsive forces. Elasticity variations on the sample surface changes the magnitude of the repulsive force, along with the phase. Mapping the phase data over a tapping mode scan results in a phase image. This image represents the elasticity variation on the sample surface. Phase imaging is not an effort towards understanding the tip-sample interaction itself. It rather provides qualitative information about sample elasticity.

It is theorized that non-linear tip-sample interaction in tapping mode generates harmonics of the cantilever's operation mode [8, 9]. Therefore, the material information is hidden in these harmonics. Since cantilever probes are operated very close to resonance in tapping mode, the response is dominated by the resonant mode and the effective bandwidth of operation is not sufficient to resolve higher frequency harmonics. Further investigation of the tapping signal in frequency domain enables reconstructing the tip-sample interaction forces [10]. However, this method may not be implemented in real-time imaging.

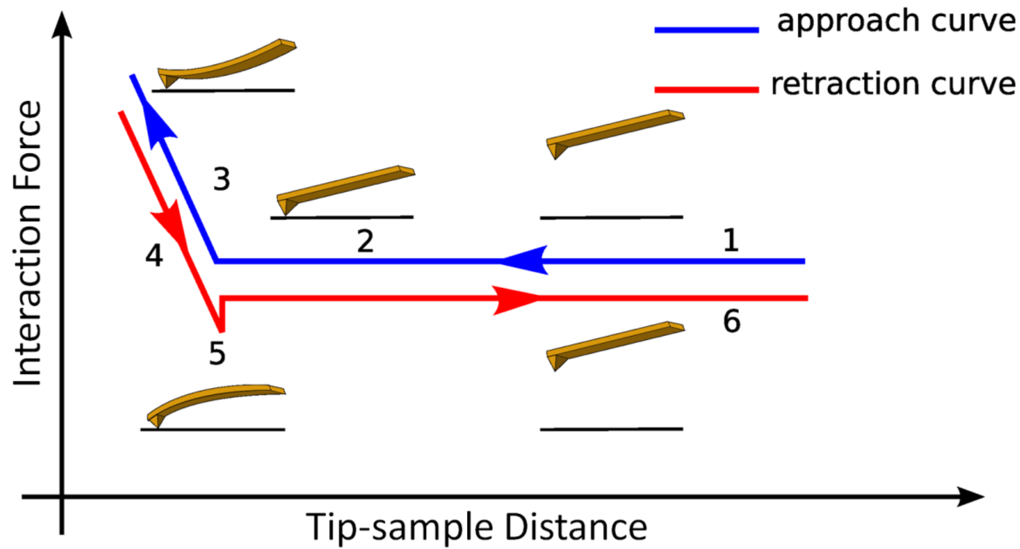

Figure 1.3 Force-distance curve measured with an AFM cantilever probe. The cantilever approaches the surface (1), jumps into contact under the effect of attractive forces (2), indents the sample surface as the repulsive forces dominate the interaction (3), starts receding from contact (4), undergoes adhesive forces before losing contact with the sample (5), moves away from the sample surface (6).

Measuring the interaction force at a single point on the sample has been conveniently available with conventional AFM systems since the early stages of the technology. By slowly approaching, contacting and lifting off the sample surface, the force exerted by the probe tip on the sample can be measured as a function of the tip-sample distance [11]. The resulting data is used to construct force-distance curves. A typical force-distance curve is depicted in figure 1.3. The cantilever approaches the sample and undergoes attractive forces before the contact is initiated. From this point on,

the repulsive regime dominates the interaction. As the repulsive forces increase, the cantilever indents further into the sample. Steps up to this point form the approach portion of the curve. After a certain repulsive force is reached, the cantilever is pulled away from the surface. The attractive forces on the tip just before losing contact with the surface are greater than the attractive forces that initiate the contact previously. This is due to adhesion hysteresis [11]. As the tip leaves the surface and recedes further, the retraction portion of the force-distance curve is complete.

Force-distance curves contain quantitative material information. In figure 1.3, the slope of the line in region (3) is correlated with the elasticity of the sample material. Additionally, the value at point (5) is the adhesion force on the tip. In an effort to incorporate force-distance curve measurements into complete scans of surfaces, force volume [12, 13] and jumping [14] modes are introduced. These modes involve raster-scanning the sample while obtaining force-distance curves at each point of contact to construct elasticity and adhesion images. The imaging time is excessive due to the fact that the force-distance curve operation is performed quasistatically at each pixel before advancing to the next pixel. The quantitative material characterization capability of force volume and jumping modes can be used with dynamic AFM techniques. In the pulsed force mode [15], the digital pulsed force mode [16, 17], and PeakForce QNM [18], a cantilever is driven much below its resonance frequency. Unlike the resonant behavior in tapping mode, this sub-resonance excitation prevents high frequency components of non-linear tip-sample interaction from being filtered out. The peak value of interaction force is maintained at a user set value to follow the topography. Meanwhile, the piezoactuator dynamically scans the surface, improving imaging time significantly over the force-distance curve methods. Additionally, Force modulation mode [19], which offers qualitative elasticity information, is combined with pulsed force mode for quantitative imaging of material properties [20]. It is also demonstrated that exciting a cantilever at a submultiple of its flexural resonance enhances the amplitude of its higher harmonics that

carry the material property information [21, 22]. These methods can be generalized as the intermittent contact mode below cantilever resonance.

Intermittent contact mode below cantilever resonance [15-18, 20-22] is performed with ordinary AFM cantilever probes. In order to manipulate harmonics generation due to non-linear tip-sample interactions, harmonic cantilevers are used [23]. These cantilevers are specially designed so that a specific higher-order flexural mode is resonant at an exact integer multiple of the fundamental resonance frequency. An SEM image of a harmonic cantilever is given in figure 1.4a. There is a rectangular opening on the cantilever that reduces the stiffness of a higher order flexural mode relative to the fundamental mode. As seen in figure 1.4b, when excited at the fundamental resonance (37.4 kHz), the 6th (240 kHz) and 16th (598 kHz) harmonics have a larger signal power compared to the other harmonics. The reason is that these harmonics are deliberately coincided with resonances of the cantilever. These enhanced harmonics can be used to image the elastic properties of samples.

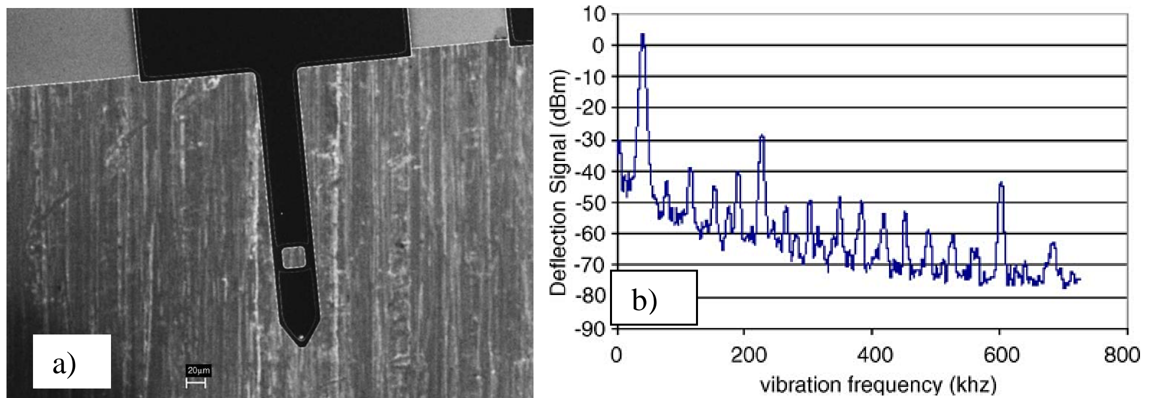

Figure 1.4 a) Harmonic cantilever with a rectangular opening. b) As the cantilever is excited at its fundamental resonance (37.4 kHz), the 6th (240 kHz) and 16th (598 kHz) harmonics are enhanced by the coinciding cantilever resonances. These harmonics are the means for imaging material properties [23].

The torsional harmonic cantilever is also used for simultaneous measurement of topography and material properties [24]. The tip is offset at the end of the cantilever as given in figure 1.5a. When the cantilever is driven by its flexural mode, due to the uneven tip configuration, the force exerted on the tip, hence the torque around the long axis

excites the cantilever's first torsional mode. This is more clearly depicted in figure 1.5b. Here, the frequency response of flexural and torsional modes of the torsional harmonic cantilever is given. The torsional response has a larger bandwidth compared to the flexural response. Therefore, the higher harmonics generated due to non-linear interaction forces are captured by the torsional mode at higher frequencies. The overall cantilever vibrations are captured by a four-quadrant photodetector. The flexural and torsional vibrations correspond to vertical and horizontal changes in the photodiode signal, respectively. The flexural vibrations are used to track topography, while the torsional vibrations are used to calculate the tip-sample interaction forces. Although harmonic [23] and torsional harmonic [24] cantilevers offer simultaneous material property imaging capabilities, some mathematical reconstruction is still required for obtaining time-resolved interaction forces.

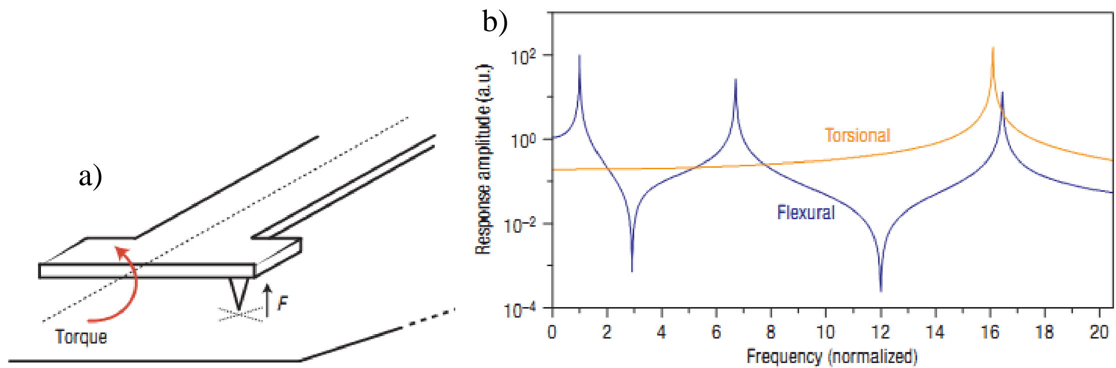

Figure 1.5 a) Torsional harmonic cantilever: Flexural vibrations are tracked for imaging topography while torsional vibrations carry interaction force information b) Flexural (blue) and torsional (orange) frequency response of the torsional harmonic cantilever: High bandwidth of torsional response enable reconstruction of interaction forces [24].

Cantilevers with integrated force sensors are able to resolve interaction forces in real-time [26]. As seen in figure 1.6a, the overall structure consists of a large cantilever with a smaller cantilever attached at the end [51]. The smaller cantilever has diffraction grating fingers for displacement detection [25]. This smaller cantilever has a higher resonance frequency than the large cantilever. When the large cantilever is resonated for tapping the surface, the small cantilever has high enough bandwidth to capture the

interaction forces. However, this method has certain limitations. One is that the vibrations of the large cantilever may couple to the small sensing cantilever. Additionally, cantilever probes are underdamped devices in general. As figure 1.6b shows, undesired coupling and lack of damping causes the cantilever to oscillate before and after contact with the sample. These oscillations cause unnecessary force on the sample which should be avoided especially during imaging of biological samples or polymers.

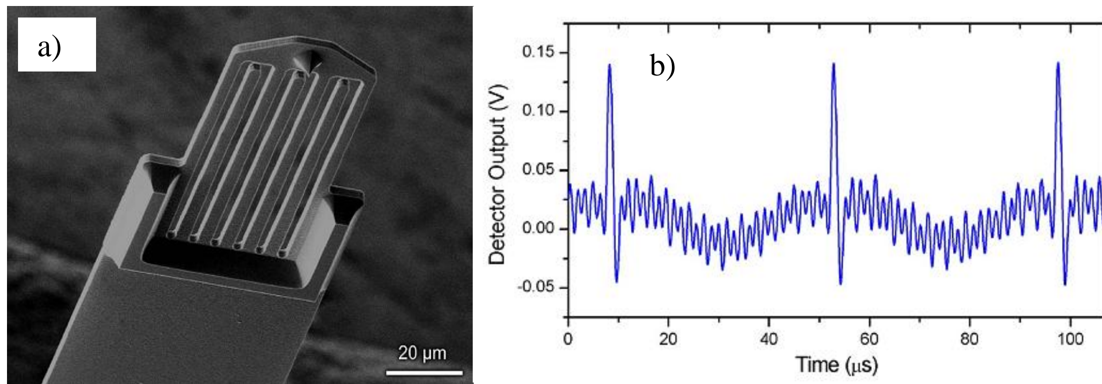

Figure 1.6 a) Cantilever with integrated force sensor: High resonance frequency of the small cantilever enables resolving interaction forces. Displacement detection is made possible by diffraction grating fingers. b) Coupling of unwanted vibrations to the sensing cantilever and lack of damping causes ringing before and after contact [26].

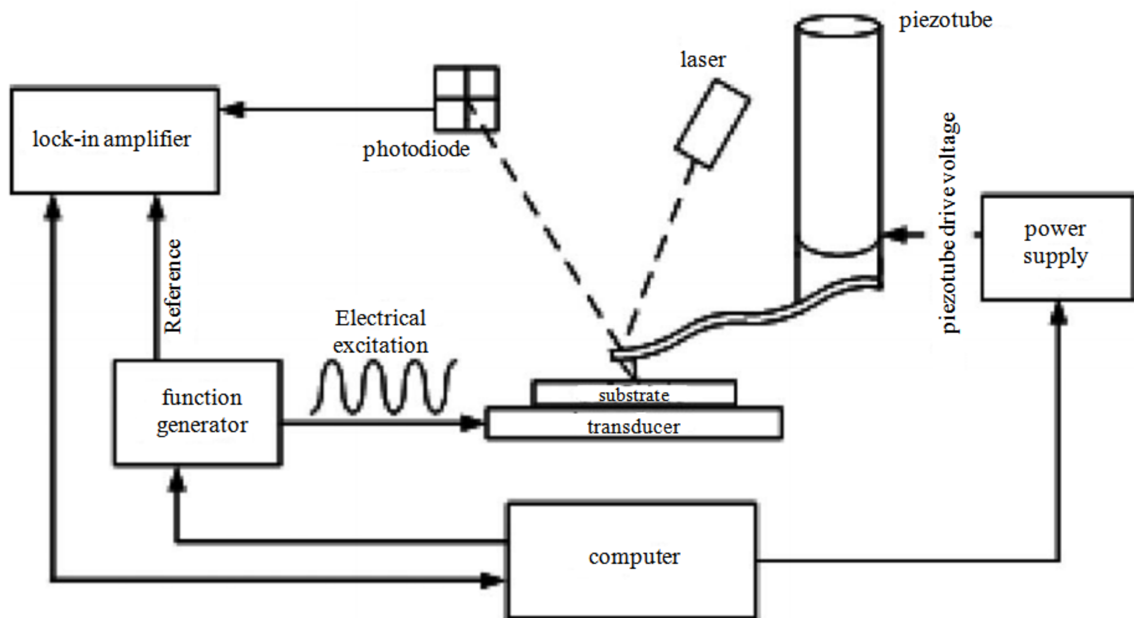

Figure 1.7 Schematic of the atomic force acoustic microscopy (AFAM) setup.

Atomic force acoustic microscopy (AFAM), a specialized imaging mode in AFM can be used for imaging elasticity [27] and subsurface defects [28] quantitatively at nanoscale. The schematic for AFAM imaging is given in figure 1.7. The sample is attached to a piezoelectric transducer, and this transducer is modulated in the vertical direction to excite the cantilever. The vibrations of the cantilever are detected by a photodiode while the cantilever tip is in contact with the sample. Shifts in flexural or torsional mode resonance frequencies of the cantilever occur due to changes in contact stiffness. Contact stiffness is a function of sample mechanical properties such as elasticity as well as the cantilever tip radius. Therefore, the shifts detected by the lock-in amplifier are linked to the elasticity variation and subsurface defects of the sample. Since this is an in-contact method, the tip wears even during a single scan, due to contact forces. Tip wear causes the tip radius to increase [27], making the contact stiffness measurements unreliable. The tip radius change can be monitored, or predicted by contact mechanics models, which adds complexity to the technique [27]. Another option is to intentionally blunt the tip before any measurements [28]. This aims to minimize the need to predict the change in tip radius.

1.2.2 Limitations

The techniques discussed so far, qualitative or quantitative, employ cantilever probes. Cantilever probes have certain limitations for simultaneous topography and material property imaging. These limitations are a result of cantilever dynamics in general. To begin with, cantilevers are passive force sensors. Therefore, in intermittent contact mode AFM measurements with cantilevers, there is always a trade-off between stable operation and force sensitivity. High resolution and low contact forces were achieved during simultaneous material property imaging with soft torsional harmonic cantilevers [29]. Here, force sensitivity is high on compliant samples, yet contact is less stable with a soft cantilever. The reason is, attractive forces on the tip may distort the

stability of tip-sample contact, and this can only be avoided by applying large tapping amplitudes or using stiff cantilevers [30]. One may use stiff cantilevers [31] or large amplitudes to improve stability, concurrently promoting tip and sample damage and loss of force sensitivity.

Cantilever probes also lack sufficient damping for dynamic operation. In intermittent contact mode below cantilever resonance [15-18], as well as the methods involving special cantilevers [24, 26]; the energy stored in tip-sample contact is dissipated through oscillations of the cantilever upon losing contact with the sample. These oscillations, also known as ‘ringing’, cause undesired forces on the sample. In addition to tip and sample damage, excessive forces on the sample may cause inaccurate measurement of topography. Consequently, it is crucial to minimize repulsive forces during imaging to avoid topography errors. Meantime, the stability of contact must be ensured by a stiff probe near attractive region of sample interaction. In order to have complete force control as well as stable operation, the stiffness of the probe needs to be actively adjusted. Rather than a passive and underdamped force sensor such as a cantilever, an active and damped probe is required for this purpose.

Limitations of a cantilever for simultaneous topography and material property imaging can be better presented by experimental data. Figure 1.8a shows the time-resolved interaction force signal when a cantilever with a stiffness of 65 N/m, resonance frequency of 282 kHz, and a Q factor of 522 is modulated at 2 kHz under peak force control to image a silicon sample. For a peak force value of approximately 400 nN, the ringing is shown to exceed 600 nN. Controlling the peak force value is not sufficient for full force control. Ideally, the tip-sample interaction force should be as given in figure 1.8b. The repulsive force is minimized, and ringing is eliminated. The contact time, the time between pull-on and pull-off points, is kept constant. This way, important material information such as elasticity and adhesion force is preserved. The ideal AFM probe that can produce such an interaction with the sample should have broad bandwidth to resolve

the interaction forces, active control capability for small interaction force and stable operation, and sufficient damping to avoid undesired forces on the sample.

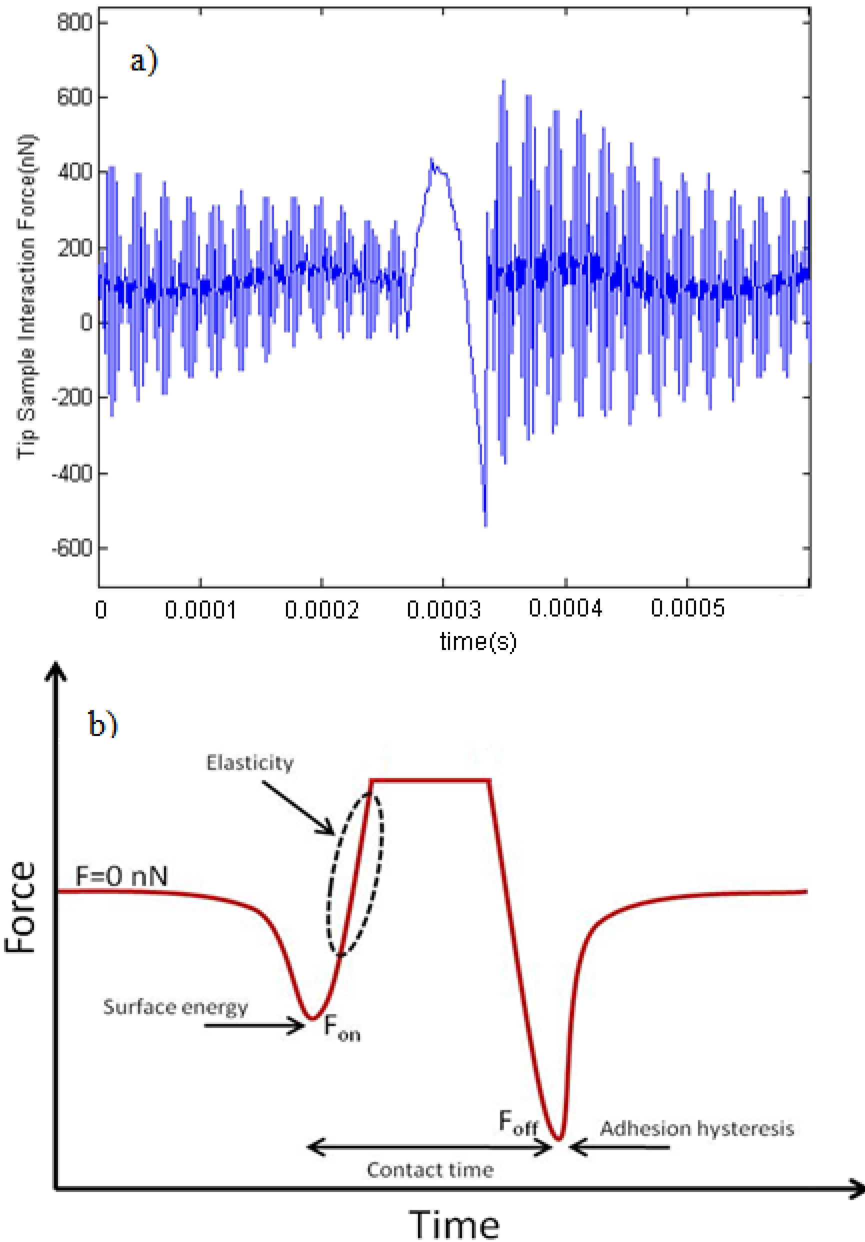

Figure 1.8 a) Time-resolved interaction force signal when a cantilever with a stiffness of 65 N/m, resonance frequency of 282 kHz, and a Q factor of 522 is modulated at 2 kHz under peak force control. Ringing exceeds peak force value. b) The desired tip-sample interaction signal during simultaneous topography and material property imaging: Repulsive force is minimized while contact time is kept constant and ringing is eliminated.

1.3 Research Goals

The purpose of this research is to analyze simultaneous topography and material property imaging in detail via numerical simulations and experiment, using passive and active AFM probes. This requires building a comprehensive AFM model that includes the fundamental elements of an AFM system. These elements are the AFM probe, the nonlinear tip-sample interaction, and the AFM z-piezoactuator. Once such a model is established, these individual elements can be modified so as to investigate various probe structures, imaging modes and tip-sample interaction theories.

In the scope of this work, Force sensing integrated readout and active tip (FIRAT) probe is chosen as an example of an active probe. FIRAT probe is a recently introduced AFM probe [32] that has been shown to solve some of the aforementioned problems [32, 35-37] associated with material property imaging at nanoscale. FIRAT probe is utilized in time-resolved interaction force (TRIF) imaging [32, 35] which takes advantage of the probe's broad bandwidth to resolve the non-linear interaction forces between the tip and the sample during simultaneous imaging of topography and material properties. FIRAT probe's sufficient damping eliminates ringing and the tip can be controlled actively by its integrated actuator [36].

In this thesis, a nonlinear model of FIRAT probe performing TRIF imaging on a sample with topography, elasticity and adhesion variations is implemented in Matlab Simulink. Other imaging modes such as TM AFM can also be simulated using this model. The model is verified for passive cantilevers by reproducing published results of TM AFM simulations [38]. Simulated TRIF mode line scans are presented in order to illuminate the effect of elasticity and adhesion variations on accurate topography measurement during simultaneous material property imaging. Passive and active tip control schemes are also simulated and the effects of these schemes are investigated in terms of stable contact and accurate material information. The results of active tip control (ATC) experiments [36] are compared with simulation results.

CHAPTER 2

FORCE SENSING INTEGRATED READOUT AND ACTIVE TIP PROBE

FIRAT probe is a broadband, active and damped AFM probe built based on a micromachined acoustic sensor membrane with integrated optical readout [33, 34]. Figure 2.1 shows a side-view schematic, and an SEM image of the FIRAT probe. It is a flexible beam with a sharp tip as the force sensor, suspended over a transparent substrate and diffraction gratings for interferometric displacement detection [32]. As the probe tip contacts the sample surface, the flexible beam deflects; changing the gap between the beam and the gratings. The incident laser beam goes through the transparent substrate and reflects both from the grating fingers and the backside of the beam to generate diffracted orders. The gap change due to beam deflection alters the intensity of the diffracted orders so that this intensity change can be used to track the displacement of the beam. The first diffraction order is captured with a photodiode for tracking the displacement of the beam. FIRAT probe inherits this detection scheme from micromachined acoustic sensor membranes [33, 46].

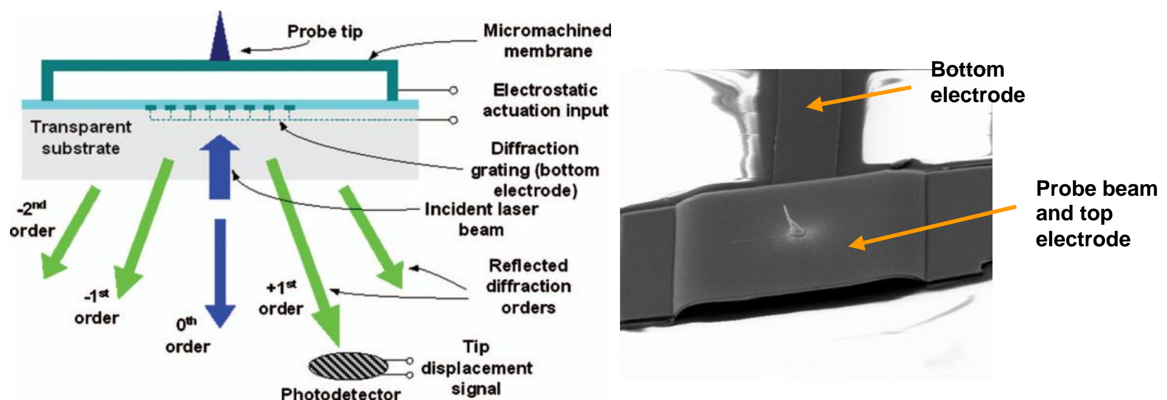

Figure 2.1 Left: Schematic cross section of the FIRAT probe for AFM studies. Right: The scanning ion beam image of an actual FIRAT probe which will be used in this project [32].

Active nature of FIRAT probe is the result of the diffraction gratings and the flexible beam serving as electrostatic actuation ports [32]. This actuation mechanism can

be used to optimize the displacement detection sensitivity. The interferometric sensitivity of the displacement measurement can be adjusted by applying a DC bias voltage to change the gap. This is demonstrated with micromachined acoustic sensor membranes [46]. As seen in figure 2.2, the output of the photodetector capturing a single diffracted order changes almost sinusoidally, as a function of the bias voltage applied between the diffraction gratings and the sensor membrane. Imperfection of the sinusoid results from the nonlinear nature of the electrostatic actuation [41]. For this particular device [46], the optimal sensitivity is available at 30, 50, and approximately 65 V. According to the characteristics of a given FIRAT probe, a suitable DC bias voltage is applied to the electrostatic actuation port during imaging experiments in order to maintain the optimal sensitivity. Adjusting the optical detection sensitivity is not possible for the cantilevers with diffraction gratings [25, 26], which were reviewed in detail previously.

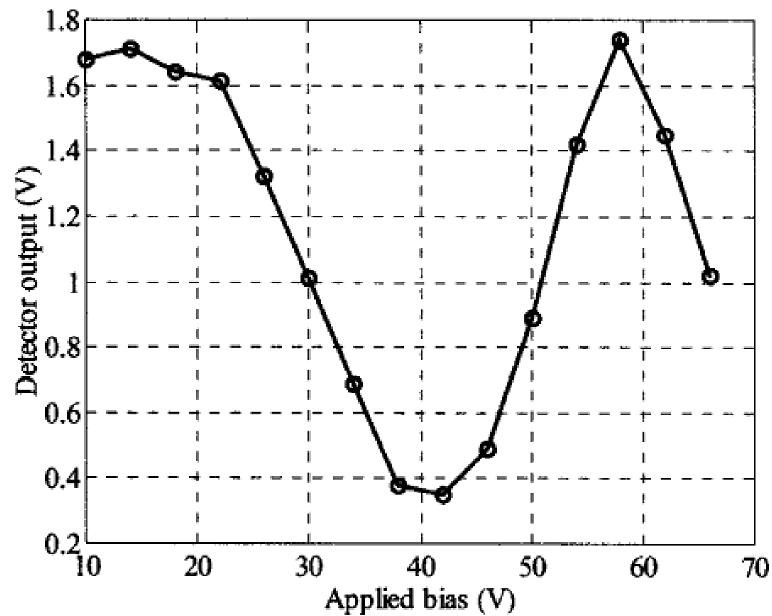

Figure 2.2 The change in photodetector output voltage as a function of the bias voltage applied between the diffraction gratings and the sensor membrane. The gap change due to applied bias alters the intensity of the first diffracted order [46].

It has been already discussed in this thesis that the non-linear tip-sample interaction generates harmonics of the probe's operation mode [8, 9]. It is possible to capture the tip-sample interaction force either with cantilever probes during intermittent

contact mode below resonance [15-18, 20-22] or with specially designed tapping mode cantilevers [23-26], yet these methods suffer certain limitations. Due to being passive force sensors, cantilever probes always have to compromise force sensitivity and sample protection for stable operation [29-31]. Lack of damping [15-18, 24, 26] is also problematic for avoiding sample damage during imaging. By means of its active nature, FIRAT probe eliminates the sensitivity-stability trade-off that the regular cantilevers have [36], and its sufficient damping prevents any unnecessary forces on the sample [32]. FIRAT probe's broad bandwidth makes it suitable for various imaging applications, as will be discussed here on.

2.1 Imaging Modes and Applications of FIRAT Probe

FIRAT probe has been used in a variety of imaging modes [32, 35-37]. These imaging modes include time-resolved interaction force (TRIF) imaging [32, 35], fast tapping mode imaging [32], and combined quantitative ultrasonic and TRIF AFM imaging [37]. In these imaging applications, FIRAT probe's broad bandwidth and electrostatic tip actuation capability has been utilized, differentiating these methods from conventional AFM techniques.

2.1.1 Simultaneous Topography and Material Property Imaging by TRIF Mode AFM

Since FIRAT probe has a broad bandwidth, the effect of harmonics generated due to non-linear tip-sample interaction [8, 9] is visible in the tip response. Therefore, time-resolved interaction forces (TRIFs) are captured by the tip displacement signal. In this imaging mode, which is called TRIF mode AFM, the probe base is moved in vertical direction by an AFM piezoactuator in order to establish tip-sample contact periodically [32]. In figure 2.3, a single tip-sample interaction cycle in TRIF mode AFM is given. Here, the tip is pulled towards the sample by attractive forces during phase I, as the

FIRAT probe approaches the sample surface. At the beginning of phase II, the tip jumps into contact and by the end of this phase, the cumulative effect of attractive and repulsive forces on the tip is zero. During phase III, the z-piezo extends until the desired force amplitude is reached, then starts retracting. The tip is pulled off the sample surface in phase IV, after experiencing adhesive forces. In phase V, the tip is moved away from the sample surface until the next interaction cycle begins. Meanwhile, the RMS amplitude of TRIFs is kept at a constant value by applying feedback control to the z-piezo. The feedback signal is used to map the topography of the sample while the TRIFs are readily available for simultaneous material characterization [32, 35].

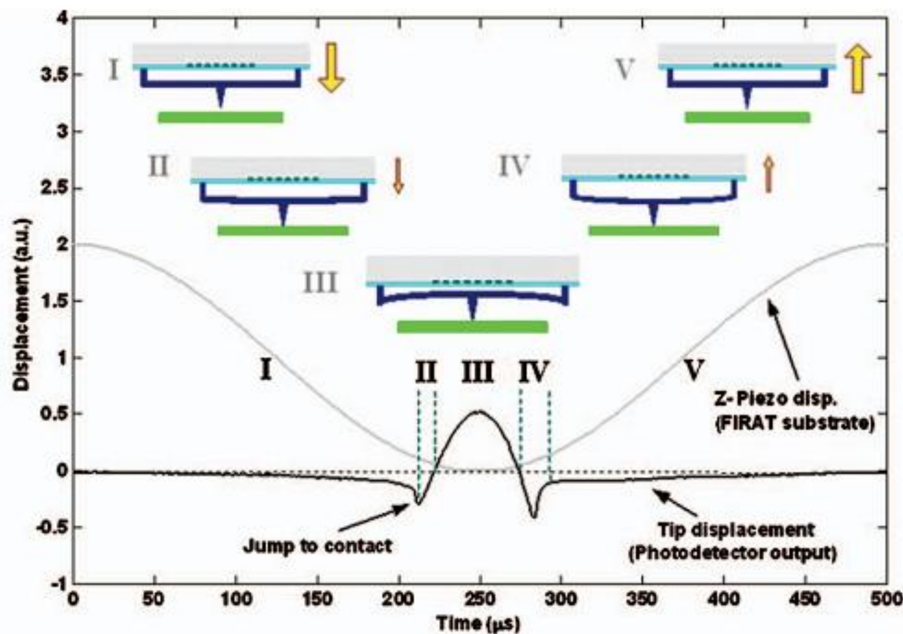

Figure 2.3 The FIRAT probe movement sequence and the resulting tip displacement signal during one cycle of contact with the sample. The z-piezo displacement that drives the FIRAT probe base is also given. As the tip approaches the sample, attractive forces pull the tip on the sample. The z-piezo extends until the desired force amplitude is reached, then retracts until the tip is pulled off the sample. The resulting photodiode output becomes the TRIF measurement [32].

Analysis of TRIFs yields valuable material information such as elasticity and surface energy. This analysis is performed by the help of an analytical tip-sample interaction model that is based on Derjaguin-Muller-Toporov (DMT) contact mechanics [35]. In figure 2.4, experimental TRIF measurements on silicon and various polymer

samples (PEGDMA, PMMA, and DEGDMA) are given. Note that, by means of its sufficient damping, FIRAT probe prevents ringing, hence unnecessary forces on the sample. According to the given experimental TRIF, the interaction model parameters are iteratively modified so that the error between the experimental and simulated TRIFs is minimized. The sample elasticity and surface energy values are available in this optimal model fit. Consequently, using the FIRAT probe, the topography and material properties of a sample can be mapped simultaneously during a single scan [32, 35].

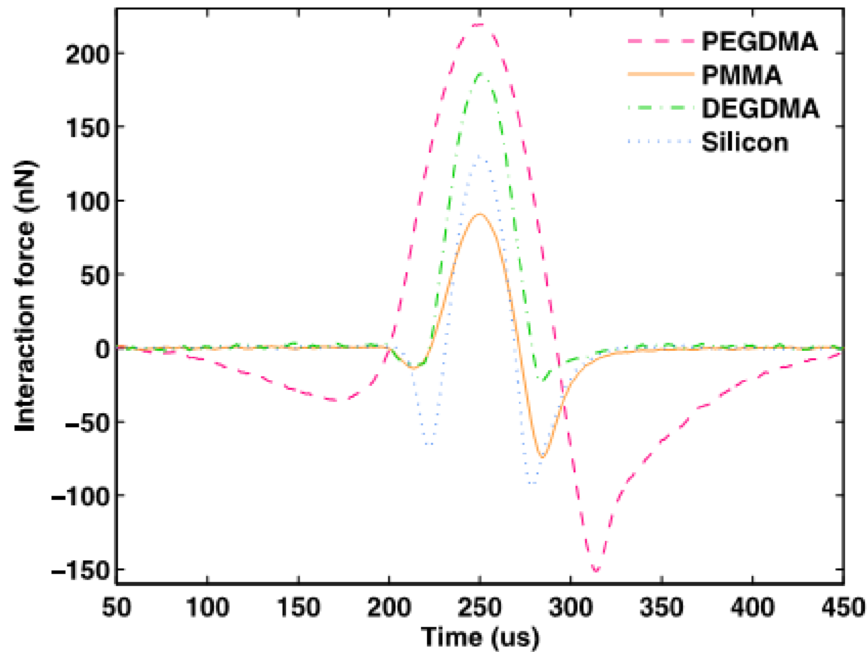

Figure 2.4 Experimental TRIFs measured by FIRAT probe on PEGDMA, PMMA, DEGDMA, and silicon samples. TRIFs contain sample elasticity and surface energy information that can be obtained using a suitable tip-sample interaction model [35].

2.1.2 Fast Tapping Mode Imaging

Tapping mode imaging [6] is advantageous for eliminating frictional forces, yet scan speed is limited by the piezoactuator scanner and cantilever dynamics. To overcome these problems, higher bandwidth piezoactuators are integrated with cantilevers and the Q factor of the cantilever is actively adjusted using the integrated piezoactuator [47, 48]. Specially designed scanners and small cantilevers with faster response are also employed for improving scan speed [49]. In addition to optimizing optical measurement sensitivity,

FIRAT probe's electrostatic actuation ports can be also utilized for fast tapping mode imaging. In order to avoid the speed limitation of an additional vertical actuator, FIRAT probe's electrostatic actuator is driven to provide the vertical tapping motion as well as the feedback control [32]. Therefore, scan speed becomes only limited by the FIRAT beam dynamics. Figure 2.5 shows tapping mode line scans of a periodic grating sample measured by FIRAT probe (a) and a cantilever probe (b) at scan rates of 1, 5, 20, and 60 Hz. In cantilever measurements, the piezo on the cantilever holder is used for tapping actuation and the feedback signal is applied to the AFM z-piezo. By means of its broad bandwidth, FIRAT probe is able to track the topography of the gratings at all scan rates, but some artifacts occur at 60 Hz. The cantilever fails to follow the steep edges of topography at 5 Hz, and it is not able to follow the actual topography of the sample at higher line scan rates [32].

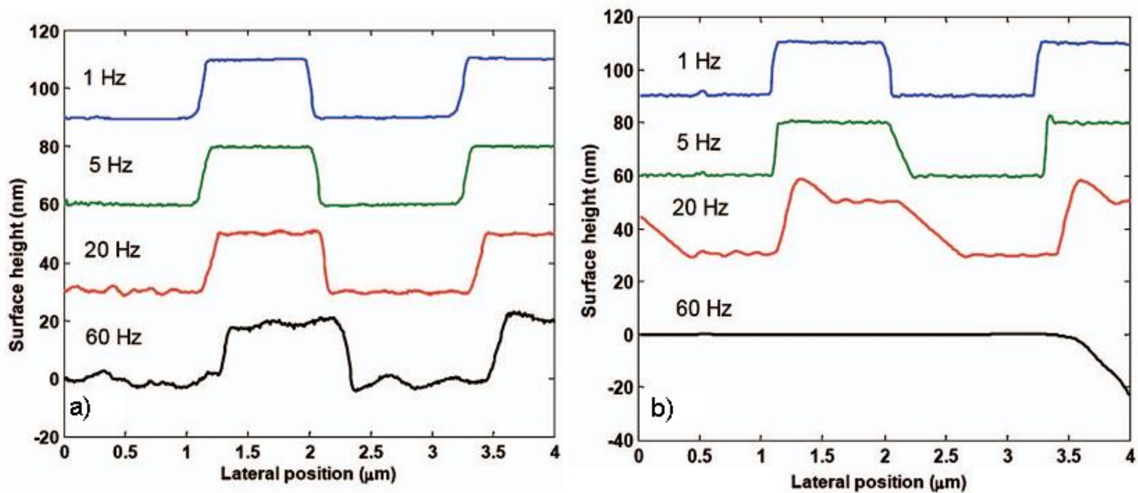

Figure 2.5 Tapping mode line scans of a periodic grating sample measured by FIRAT probe (a), and a cantilever probe (b). FIRAT probe is able to track the topography of the gratings at all scan rates, with some artifacts at 60 Hz. The cantilever fails to follow the steep edges at 5Hz, and the measurements do not reflect the actual topography of the sample at higher scan rates [32].

2.1.3 Combined Quantitative Ultrasonic and TRIF AFM Imaging

Measurement of TRIFs during intermittent contact AFM [23, 24, 32, 35] provides simultaneous mapping of topography, elasticity, and surface energy. This method is preferred for compliant samples in order to prevent sample damage. However, elasticity

measurement sensitivity degrades especially on stiff samples since sensitive measurement requires matching the probe stiffness with the contact stiffness. Therefore, ultrasonic AFM (UAFM) is employed on stiff samples [27, 28] since the effective probe stiffness is increased in this mode [50] which enhances sensitivity. This approach is not suitable for compliant samples, for the fact that UAFM involves continuous tip-sample contact which promotes sample damage. For these reasons, TRIF imaging and UAFM are combined in the same mode of operation for sensitive and nondestructive characterization of samples with large elasticity variations [37]. In this technique, FIRAT probe is operated under TRIF mode while the probe is also actuated electrostatically by a small amplitude signal at very high frequency. Any change in sample elasticity alters the contact stiffness, hence the amplitude of the small UAFM vibrations of the tip. This UAFM amplitude can be tracked to map the elasticity of the sample. Note that the topography and material property imaging capabilities of TRIF mode is concurrently available in this technique. Figure 2.6 shows elasticity measurements on an aluminum-silicon-chromium sample by TRIF mode and combined UAFM and TRIF imaging. On the silicon surface for which the expected elasticity is 52 GPa, the combined UAFM and TRIF measurement is shown to have 2.5 GPa standard deviation. In contrast, TRIF measurement provides 14.9 GPa standard deviation due to low stiffness of the probe at the TRIF mode frequency which does not match the sample stiffness. The combined method offers five times improvement over only employing TRIF mode [37].

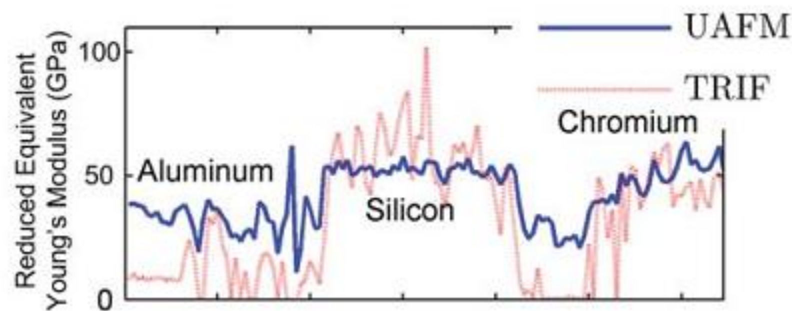

Figure 2.6 Elasticity measurements on an aluminum-silicon-chromium sample by TRIF mode and combined UAFM and TRIF imaging. TRIF mode measurement shows larger standard deviation due to non-matching probe-sample stiffness at the TRIF mode frequency [37].

2.1.4 Active Tip Control

As discussed earlier, FIRAT probe is employed in a variety of imaging modes. By means of FIRAT probe's broad bandwidth, TRIFs can be monitored during these imaging modes. Having access to TRIF signals during imaging, the interaction forces can be analyzed and the FIRAT probe tip can be electrostatically actuated in order to obtain the desired tip-sample interaction. In figure 2.7a, FIRAT probe movement sequence and the corresponding TRIF signal during one interaction cycle is given. Different phases of this interaction cycle are explained in detail earlier in this chapter. Once the repulsive force exceeds a user defined force threshold, an active control signal is generated (figure 2.7b) based on the excess force. This signal is applied to the tip electrostatically so that it is pulled away from the sample without loss of contact and the repulsive force is limited at a desired value (figure 2.7c). This approach, active tip control (ATC), is applicable to any of the imaging modes discussed in this chapter since TRIF measurements are available during these modes. By employing ATC, the probe is stiff against attractive forces and soft enough in the repulsive region. Therefore, one does not have to sacrifice stability for reducing sample indentation during imaging [36].

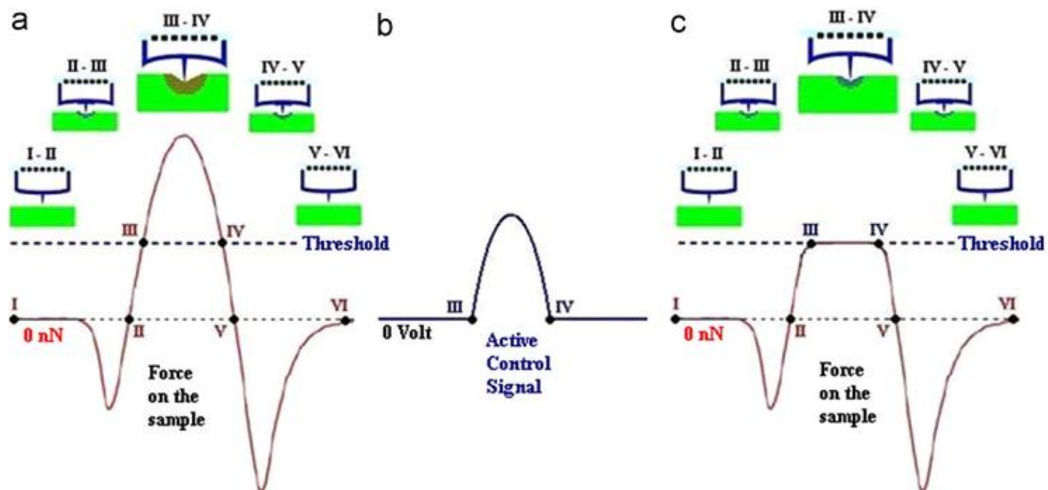

Figure 2.7 a) FIRAT probe movement sequence and the corresponding TRIF signal during one interaction cycle. b) Once the repulsive force exceeds a user defined force threshold, an active control signal is generated. c) Active control signal is applied to the tip electrostatically so that it is pulled away from the sample without loss of contact and the repulsive force is limited at a desired value [36].

2.2 Summarizing Remarks

Although FIRAT probe's imaging capabilities have been demonstrated experimentally [32, 35-37], these applications have not yet been analyzed in detail by models. A comprehensive AFM imaging model is built that can simulate various imaging modes with different probe structures. This model is used to analyze TRIF mode imaging with active probes in detail, by investigating the effect of active and passive tip control schemes as well as different sample material properties. The modeling effort is explained in the next chapter.

CHAPTER 3

MODELING TIME-RESOLVED INTERACTION FORCE MODE IMAGING

This chapter deals with modeling each of the individual components of an AFM system and incorporating them in a Simulink model. To have a general and complete imaging model, the active probe, the nonlinear tip-sample interaction, and the AFM z-piezoactuator are modeled as separate modules. Therefore, these modules can be modified easily to implement different probe structures, imaging modes or interaction models. Here, FIRAT probe is chosen as an example of an active probe. However, other probe structures such as piezoelectric cantilevers [39, 40] can be integrated with the model as well.

Figure 3.1 shows the experimental setup for AFM imaging with FIRAT probe. Two different imaging modes, TRIF mode and TM AFM are represented by solid black and dashed green lines, respectively. In TRIF mode experiments, the FIRAT tip periodically interacts with the sample by means of a sinusoidal piezo motion, and the TRIFs are monitored utilizing the intensity change of the 1st diffracted order. The peak or RMS value of the TRIFs is maintained at a desired value through PID feedback [32]. The vertical drive signal is directly applied to the piezoactuator in TRIF mode, unlike TM AFM where the probe is directly excited. In TM AFM, the feedback signal is generated depending on the RMS amplitude of resonant probe oscillations and this signal is the only one fed to the piezoactuator. ATC circuitry can be activated during TRIF mode in order to generate the electrostatic actuation force signal required to keep the repulsive force constant during each interaction cycle. This operation is represented by dash-dot red lines in figure 3.1. The peak/RMS detection, ATC and PID operations are implemented by

both analog circuits and programming a National Instruments FPGA. Both options are available for use with this setup. The details on the analog circuitry and the FPGA algorithm are given in Appendix A.

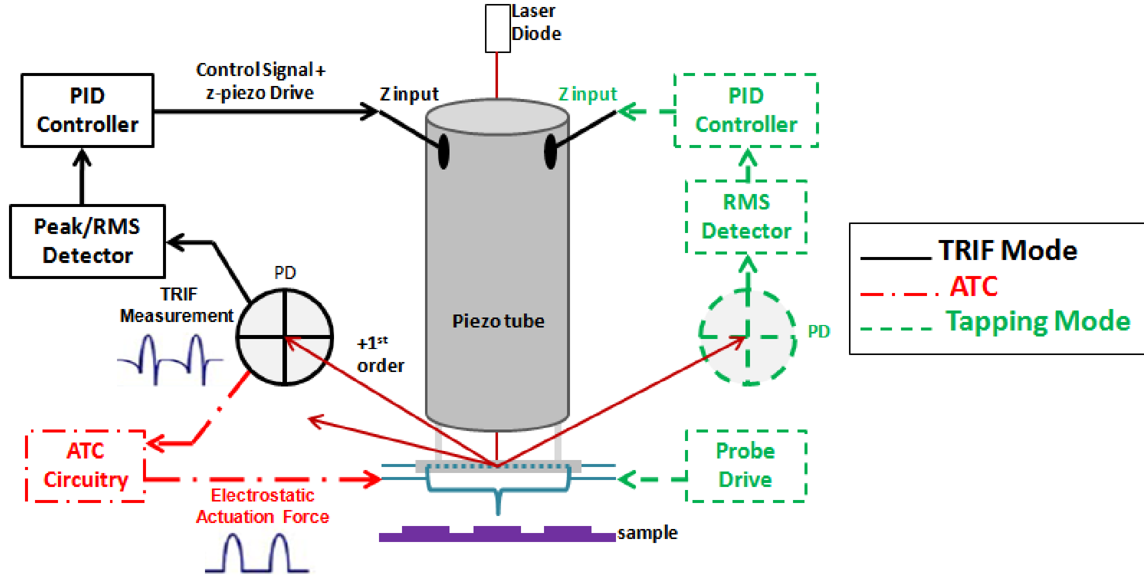

Figure 3.1 Experimental setup of time-resolved interaction force (TRIF) mode imaging, active tip control (ATC), and tapping mode AFM (TM AFM) operations using the FIRAT Probe.

3.1 FIRAT Probe Dynamics

To model the FIRAT probe, a mechanical lumped system approximation is used. This approximation is valid since FIRAT probe exhibits linear motion for small displacement amplitudes. Electrical counterparts of mechanical elements are used to form an equivalent circuit. The equivalent circuit model is given in figure 3.2. As Senturia analyzes in detail [41], the mass m, and the stiffness k of the probe are represented by an inductor and a capacitor respectively. In ambient conditions, air fills the gap between the doubly-clamped beam and the substrate. Movement of the beam, hence the gap change alters the air pressure underneath the beam. The air flow into and out of the cavity due to pressure change causes a dissipative mechanical effect on the force sensor, called the squeezed-film damping [41]. Therefore, the damping of the FIRAT structure is composed of both the squeezed-film effect and the mechanical loss in the beam itself. This additional source of damping differentiates the FIRAT probe from underdamped AFM

probes. Since the compressed air stores potential energy as well as providing additional damping, the squeezed film effect can be represented by a parallel capacitor and resistor pair. Note that, the effect of tip geometry is not included in this model. The damping constant b, in such a case is given by equation 3.1.

$$b = \frac{96\eta L W^3}{\pi^4 {g_0}^3} \qquad [17]\ (3.1)$$

Here, η is viscosity, g_0 is the gap, L and W are length and the width of the beam, respectively. Note that squeezed-film damping is both dependent on the fluid properties and probe geometry. For frequencies lower than the cut-off frequency ω_c, the impedance of the film capacitor decreases and damping dominates the film response. The film behaves as a spring for frequencies higher than ω_c, when the film resistor impedance becomes negligible compared to the capacitor impedance. The cut-off frequency ω_c is a function of the gap (g_0), the ambient pressure (P_0), the viscosity (η), and the width of the beam (W):

$$\omega_c = \frac{\pi^2 {g_0}^2 P_0}{12\eta W^2} \qquad [17]\ (3.2)$$

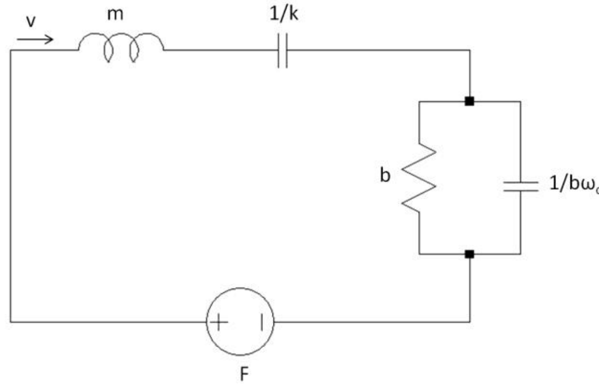

Figure 3.2 Lumped Element Model of the FIRAT Probe.

According to the $e \rightarrow V$ convention, the across variable of the circuit is force (F), and the through variable is the velocity (v) of the beam. The transfer function from applied force (F) to tip displacement (x) can be deducted from the equivalent circuit as:

$$\frac{x(s)}{F(s)} = \frac{\frac{s}{\omega_c} + 1}{\frac{ms^3}{\omega_c} + ms^2 + \left(b + \frac{k}{\omega_c}\right)s + k} \tag{3.3}$$

Equation 3.3 can be rewritten as in equation 3.4, substituting $j\omega$ for s. Therefore, the effect of film cutoff frequency ω_c on the probe response is more evident.

$$\frac{x(j\omega)}{F(j\omega)} = \frac{\frac{j\omega}{\omega_c} + 1}{\frac{m(j\omega)^3}{\omega_c} + m(j\omega)^2 + \left(b + \frac{k}{\omega_c}\right)j\omega + k} \tag{3.4}$$

Then, the damping term in the denominator becomes $bj\omega + kj\omega/\omega_c$. If the film cutoff ω_c is larger than the operating frequency ω, the damping term is dominated by the $bj\omega$ term. This means the squeezed-film behaves as a damper. If the film cutoff ω_c is smaller than the operating frequency ω, the same term becomes $kj\omega/\omega_c$ and the spring effect dominates.

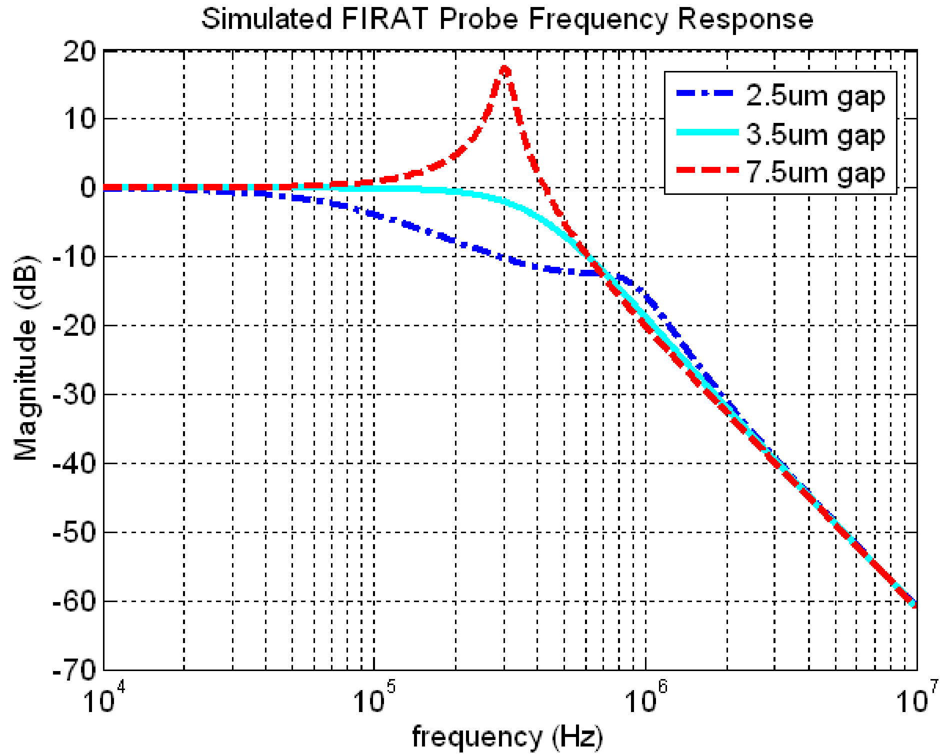

Figure 3.3 Simulated frequency response of FIRAT Probe for different gaps. Damping of the probe increases due to squeezed-film effect, as the gap decreases.

In addition to operating frequency, another component that determines the probe response is the probe gap. As equation 3.1 indicates, damping has an inverse relationship with gap. Figure 3.3 shows the simulated frequency response of FIRAT probe for different gaps. The probe with 2.5 µm gap has a damped response whereas the 7.5 µm gap results in a more resonant device. For the sake of eliminating repulsive forces caused by transient ringing during imaging, a damped probe is desired. However, a trade-off exists between the damping and the bandwidth of the probe. In the case of the 2.5 µm gap, the damping is so high that the usable bandwidth of the probe decreases. In contrast, the 3.5 µm gap yields the optimal bandwidth while still providing sufficient damping that eliminates ringing.

3.2 Tip-Sample Interaction Model

In intermittent contact mode AFM such as TRIF imaging or TM AFM, the tip approaches the sample, goes into contact with the sample, and is separated from the sample in a periodical manner. While the tip is approaching the sample, it undergoes attractive forces such as van der Waals and electrostatic forces. Although attractive forces are still present after the tip jumps into contact, the repulsive forces start to dominate as the z-piezo extends to reach a force set point. When the set point force is met, the tip starts to recede, experiencing adhesion forces until it is finally pulled off the surface. The force required to break tip-sample contact is larger than the force that initiates the tip-sample contact. This is called adhesion hysteresis. Adhesion hysteresis may be caused by the probe instabilities, chemical bonding, and plasticity [42]. Here, a theoretical model that includes different phases of the tip-sample interaction is presented.

3.2.1 Contact Mechanics Models

Theoretical contact mechanics models are essential for material property imaging for the fact that they are used to invert tap signals in order to determine material

properties such as effective elastic modulus. For simulation purposes, it is also important to choose a theoretical contact mechanics model that suitably represents the AFM tip-sample interaction and also is computationally favorable.

3.2.1.1 Hertzian Contact Model

Hertzian contact model represents elastic contact between a sphere body and a flat surface. This model only accounts for repulsive forces and does not include the effect of attractive surface forces. The interaction force between the sphere body and the flat surface is represented by:

$$F = E^{*}\delta^{1.5}R^{0.5} \tag{3.5}$$

Where, F is the interaction force, E^{*} is the reduced tip-sample elastic modulus, δ is the indentation, and R is the tip radius. As given in equation 3.6, the reduced tip-sample elastic modulus E^{*} is a function of the Poisson ratio ν, and the elastic modulus $E$of both the tip and the sample.

$$\frac{1}{E^{*}} = \frac{3}{4}\left[\left(\frac{1-{\nu_{tip}}^{2}}{E_{tip}}\right)+\left(\frac{1-{\nu_{sample}}^{2}}{E_{sample}}\right)\right] \tag{3.6}$$

3.2.1.2 Derjaguin-Muller-Toporov (DMT) Contact Model

DMT contact model builds on Hertzian theory. The force calculation is modified such that attractive surface forces are included in the model, hence the tip-sample interaction can be more realistically represented. Equation 3.7 gives the interaction force.

$$F = E^{*}\delta^{1.5}R^{0.5} - 2\pi R\varpi \tag{3.7}$$

While the first term is the repulsive force from Hertz contact theory, the second term introduces the effect of attractive surface forces, where ϖ is the surface energy per unit area. The range of the surface forces and the tip-sample separation are assumed to be much smaller than the tip radius [42].

DMT model does not account for the adhesion hysteresis. Additionally, the interaction force has a discontinuity at the point of initial contact. For these reasons,

DMT model is not the ideal contact mechanics model for representing the real tap signals. However, it is the preferred method for inverting the reduced elastic modulus information from tap signals due to being computationally inexpensive.

3.2.1.3 Burnham-Colton-Pollock (BCP) Contact Model

BCP mechanics includes the effect of long range attractive forces in the contact model. The equations that represent the tip-sample contact mechanics are:

$$F = \frac{E^* a^3}{R} - \pi R \overline{\omega} - \sqrt{\frac{3\pi \overline{\omega} E^* a^3}{2}} \tag{3.8}$$

$$\delta = \frac{a^2}{R} - \left(\frac{\pi^2 R \overline{\omega}^2}{E^{*2}} \right)^{1/3} \tag{3.9}$$

Here, a is the contact radius. When compared to the DMT model, it can be seen from the second term in equation 3.8 that the effect of attractive surface forces is decreased. This is due to the role of long range attractive forces in the model. The third term represents the attractive force that causes the surface geometry to bulge outward during the non-contact phase. Similarly, the second term in equation 3.9 is the outward displacement of the sample towards the tip. This behavior provides a smooth transition between non-contact and contact forces in contrast to the discontinuity in the DMT model. BCP model better represents the tapping event than the DMT model, but material property inversion is not as practical. Adhesion hysteresis is also not part of the BCP contact mechanics [42].

3.2.1.4 Johnson-Kendall-Roberts-Sperling (JKRS) Contact Model

JKRS mechanics includes adhesion hysteresis in the tip-sample interaction model. The attractive forces that keep the tip and the sample in contact are larger in magnitude than the attractive forces that cause the tip to jump into contact with the sample.

$$F = \frac{E^* a^3}{R} - \sqrt{6\pi\overline{\omega}E^* a^3} \quad (3.10)$$

$$\delta = \frac{a^2}{R} - \frac{2}{3}\sqrt{\frac{6\pi\overline{\omega}a}{E^*}} \quad (3.11)$$

Unlike DMT, and BCP contact mechanics, the force is zero before tip-sample contact. Long range attractive forces are ignored, but surface attractive forces are apparent just after contact. JKRS model is a suitable representation for highly adhesive systems with large contact radius [42].

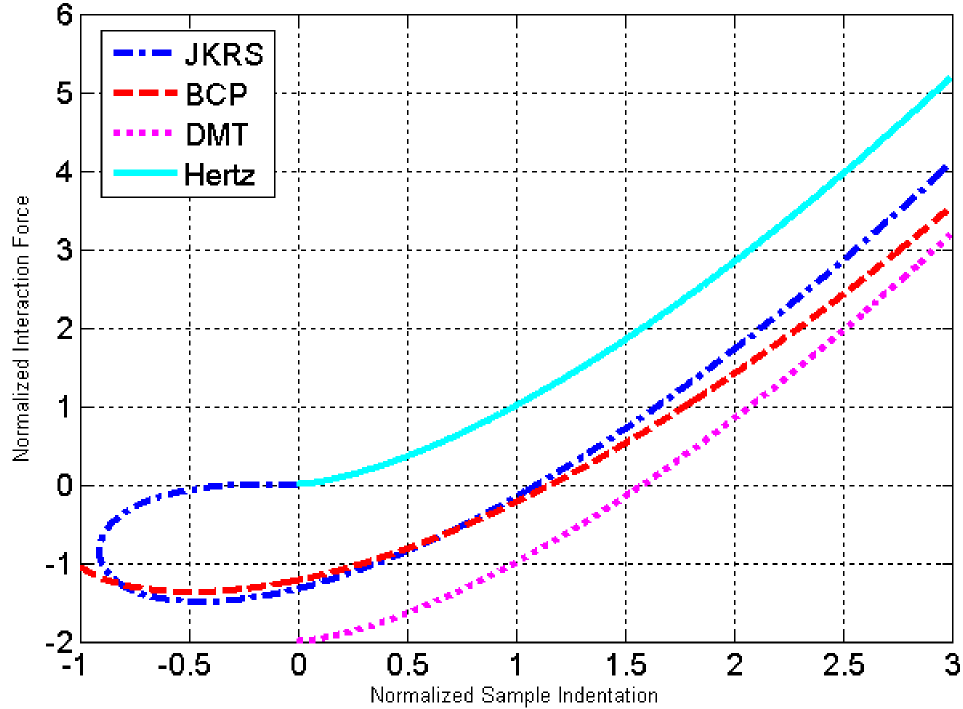

Figure 3.4 Comparison of Hertz, DMT, BCP and JKRS contact mechanics models.

3.2.2 Comparison of Contact Mechanics Models

The information given above is summarized in figure 3.4. The Hertz model (solid line) only calculates force when the tip and the sample are in contact. DMT model (dots) adds the effect of short range attractive forces, thus it is an offset version of Hertz. Note that there is no force value assigned to the region where the tip and the sample are out of

contact. This causes a discontinuity at the jump-into-contact point. BCP model (dashed line) accounts for attractive forces in the non-contact region. This is possible through assuming negative sample indentation, meaning that the sample bulges outward. By including attractive forces, BCP model offers a continuous transition between non-contact and contact regions. None of these models account for adhesion hysteresis, except for JKRS (dash-dot). Among these models, DMT model is the most computationally inexpensive choice for inverting elasticity information. Therefore, combining DMT with separate attractive force models is a suitable method for modeling TRIFs.

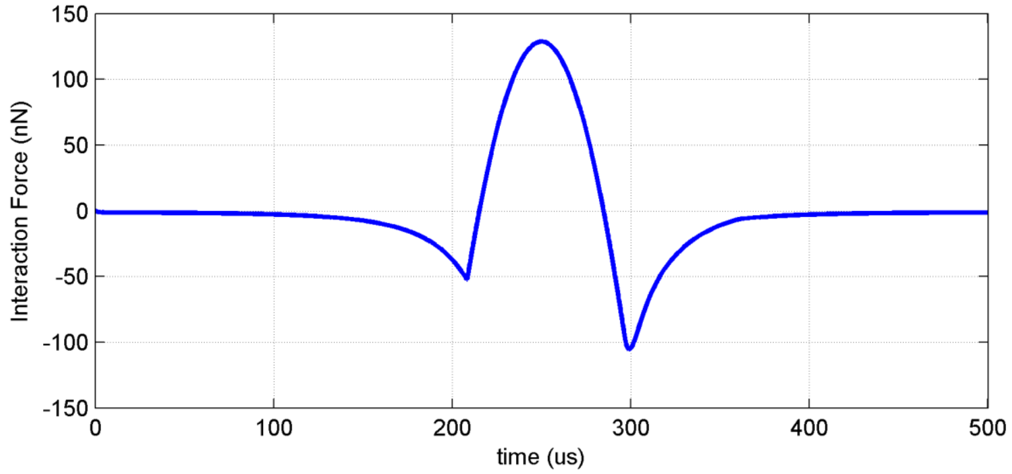

Figure 3.5 Simulated TRIF signal of FIRAT probe using the constructed interaction model.

3.2.3 The Interaction Model via Contact and Non-contact Forces

The attractive interaction between the tip and the sample can be modeled as a combination of the van der Waals forces and the patch charge within the probe tip [35]. By combining attractive and repulsive interactions, the overall interaction force model is obtained, as given in equation 3.12.

$$F(d) = \begin{cases} \dfrac{-2\pi R\overline{\omega}}{(1+\frac{d}{Z})^{2}}, & d \geq 0 \\ E^{*}\sqrt{R}(-d)^{\frac{3}{2}} - 2\pi R\overline{\omega}, & d < 0 \end{cases} \tag{3.12}$$

Here, *d* is the tip-sample distance. The distance between the patch charge in the tip and the tip end is represented by *Z*. The attractive forces still behave like van der Waals forces due to the squared term in the denominator, with the added effect of the patch charge. The transition from non-contact to contact region is made possible by setting attractive and repulsive forces equal to each other when $d=0$. Adhesion hysteresis is included in this model by assigning a larger surface energy value to the force equation during tip retraction from the sample surface.

Figure 3.5 shows a simulated TRIF signal that is constructed using the interaction model explained above. As the tip approaches the sample surface, the attractive forces cause the FIRAT probe to deflect towards the sample. According to the interaction model, attractive forces equal repulsive forces when the tip jumps into contact. A discontinuity occurs at this point since DMT contact model does not calculate non-contact forces. The repulsive forces on the tip increase as the tip indents the sample surface. When a certain maximum repulsive force value is reached, the tip recedes from the surface, experiencing adhesive forces before losing contact with the sample. Due to adhesion hysteresis, the force required to retract the tip from the surface is larger than the attractive force that pulls the tip into contact.

3.3 Experimental Characterization of the Atomic Force Microscope Piezoactuator

Unlike TM AFM, which can be simulated without including the effect of piezoactuator dynamics [38, 43]; the z-piezoactuator drives the probe directly in TRIF mode. Therefore, the z-piezoactuator should also be modeled and included in the overall model in order to simulate the TRIF operation of FIRAT probe realistically. In addition, including the z-piezoactuator dynamics in the model is required for investigating the effect of scan rate on topography measurements.

Due to complex geometry and material properties of the piezoactuators, it is challenging to model them in a completely theoretical manner. Therefore, experimental

characterization is a convenient choice. This method has been utilized for performing system identification on piezoactuators and developing various control strategies for AFM systems [44, 45]. The magnitude and phase response of the E type piezotube of Multimode SPM (Digital Instruments Veeco Metrology Group) is measured, sweeping from near DC to 25 kHz. Then, a 5th order transfer function is fit to the experimental data by means of Matlab's 'oe' function. The experimental frequency response of the piezoactuator in vertical direction and the corresponding transfer function fit are given in figure 3.6.

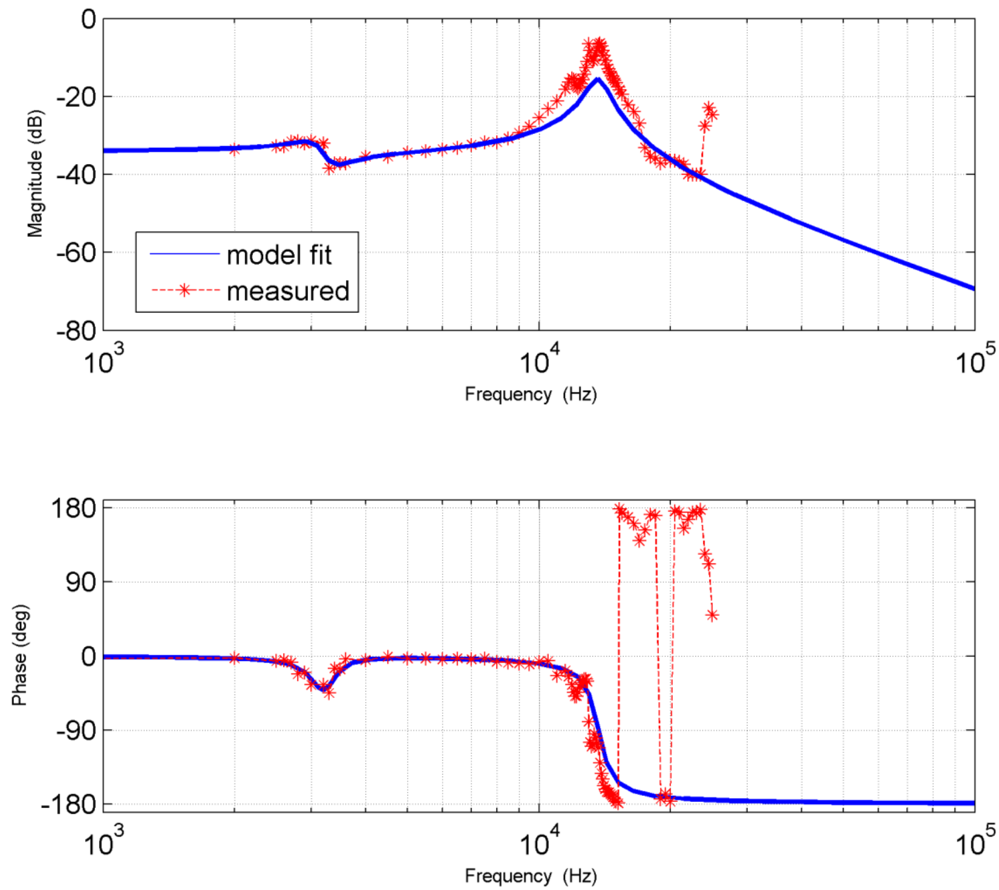

Figure 3.6 Magnitude (top) and phase (bottom) response of the Multimode SPM piezoactuator as a function of frequency. The red asterisk represents the experimentally measured response. The blue solid line is the model fit to experimental data.

The transfer function fits the experimental values quite well below 10 kHz. The model magnitude is slightly smaller than the peak at 13.8 kHz. There are also two smaller peaks near the main peak, at 12 kHz and 13 kHz which are not included in the model. In addition, the experimental phase data is more complex than the model phase after 10 kHz. Differences between the model and the experimental data are due to the fact that the actual order of the system is higher than 5. One has to choose a higher order for the transfer function in order to fully comply with the higher frequency dynamics. Since the tapping frequency is 2 kHz in the TRIF imaging simulations, a 5th order transfer function is sufficient for representing the z-piezo dynamics for the frequency of interest.

3.4 Combined Simulink Implementation of the Imaging Model

The probe, tip-sample interaction, and the z-piezoactuator models are combined with the remaining elements of an AFM imaging experiment in order to construct a Simulink model. Figure 3.7 shows the Simulink model to simulate imaging with FIRAT probe, and it is an important schematic to understand. The legends shown in figure 3.1 also apply to figure 3.7. TRIF mode imaging is represented by the solid black lines. In TRIF mode simulations, the z-piezo is driven sinusoidally at 2 kHz to move the probe base. Depending on the surface topography, the tip-sample distance is calculated. This tip-sample distance information determines whether the tip is in the attractive or the repulsive region. Tip-sample distance and the sample material properties are used by the tip-sample interaction model to calculate the force on the tip. This force is then fed to the probe transfer function to obtain the tip displacement. Note that tip displacement value is combined with the probe base displacement and the surface topography to calculate the tip-sample distance. The tip displacement is multiplied by a force sensitivity to obtain the TRIF measurement. The TRIF measurement is evaluated by the peak detector and the desired peak force is maintained by applying a PID control signal to the z-piezoactuator

model. Alternatively, an RMS detector can be used if the feedback parameter of interest is the RMS amplitude of TRIF. At this point, the imaging loop is closed.

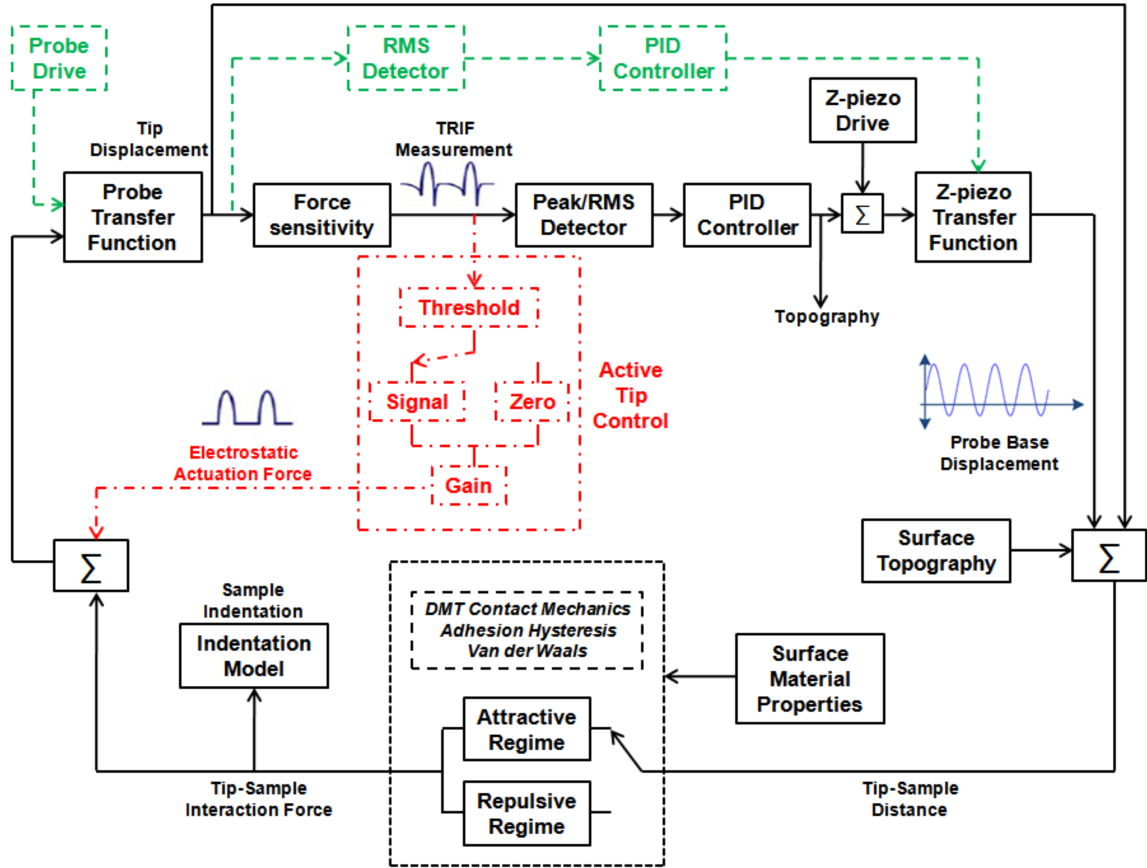

Figure 3.7 Simulink model of time-resolved interaction force (TRIF) mode imaging, active tip control (ATC), and tapping mode AFM (TM AFM) operations using active and passive probes**.**

Additionally, sample indentation is calculated using the repulsive force. The indentation is represented by equation 3.13. According to Hertz contact theory, the indentation, h, is defined by the repulsive force F_{rep}, the reduced Young's modulus, E^* and the tip radius, R. Here, DMT contact mechanics is used; therefore the sample indentation must be calculated accordingly. As an addition to Hertz theory, DMT model includes the effect of short range attractive forces in the contact force. Therefore, the repulsive force becomes $F_{rep} = F_c + 2\pi R\varpi$, where F_c is the contact force given by equation 3.12 when $d<0$. Simultaneous calculation of sample indentation (equation 3.13) is a sanity check to the amount of topography measurement error.

$$h = \sqrt[3]{\frac{{F_{rep}}^2}{{E^*}^2 R}} \tag{3.13}$$

The model explained above is an effort to analyze AFM in general. It can be modified for other imaging conditions or additional functionalities can be introduced. For instance, conventional TM AFM imaging can be simulated with this model by including a cantilever transfer function and exciting the probe near its resonance frequency. This case is represented in figure 3.7 by dashed green lines. Other tip-sample interaction models such as Burnham-Colton-Pollock (BCP) or Johnson-Kendall-Roberts-Sperling (JKRS) can be used instead of DMT [30]. If active probes such as FIRAT probe or piezoelectric cantilevers [39, 40] are used, the probe tip can be actively controlled as shown in figure 3.7 with the dash-dot red lines. In this case, once the TRIF measurement exceeds a user-defined threshold, the ATC block generates a control signal which feeds the excess force back to the probe transfer function to keep the repulsive force at the desired value [36]. ATC aims to actively soften the probe which limits the sample indentation, hence reduce topography measurement errors.

CHAPTER 4

SIMULATION RESULTS AND EXPERIMENTAL VERIFICATION

Using the model explained in Chapter 3, various imaging modes, probe structures, sample material properties, tip-sample interaction force models, and actuation and feedback schemes can be investigated. This chapter shall discuss the accurate topography measurement of samples with elasticity and adhesion variations during peak force and RMS control. Additionally, passive and active tip control schemes for simultaneous topography and material property imaging are put to test by the imaging model. The FIRAT probe properties and other parameters used in simulations are given in table 1. Experimental verifications of the simulation results are provided.

Table 1 FIRAT Probe Properties and Imaging Parameters Used In Simulations

Parameter	Value
Length, L	80 μm
Width, W	80 μm
Thickness, t	0.4 μm
Gap, g_0	2.5 μm
Beam density, ρ	2700 kg/m^3
Stiffness, k	25 N/m
Tip radius, R	15 nm
Distance from the patch charge to the tip end, Z	20 nm
Viscosity of air, η	1.78*10^{-5} kg/m*s
Ambient pressure, P_0	101.325 kPa
Piezo movement amplitude, Y_0	57.5 nm
TRIF mode operation frequency, f	2 kHz

4.1 Effect of Elasticity Variations on Accurate Topography Measurement of Samples

To simulate the effect of elasticity variations on topography measurement, we use the sample topography given in figure 4.1. Here, the defined sample topography is represented by the blue line. The lower region of the sample is stiff (E^*=100 GPa) and the higher region is much softer (E^*=2 GPa). The adhesion of the sample is constant

throughout. TRIF mode topography measurement of this sample with FIRAT probe is simulated. The type of feedback is chosen as peak force control. The discontinuous lines in figure 4.1 represent the measured topography of the defined sample with different peak force values. As the tip arrives at the step, the tip offset from the sample surface decreases. Since the z-piezo movement amplitude remains unchanged, the force applied to the sample by the tip increases. When the peak value of the interaction force exceeds the desired peak force value, the PID controller adjusts the feedback signal to retract the z-piezo away from the surface. The z-piezo is retracted until the peak force value becomes the desired one. The feedback signal generated by the PID controller block (figure 3.7) during the imaging simulation is plotted as measured topography after being multiplied by an appropriate conversion factor. The larger the peak force, the larger the error in topography measurement. The topography error in each case amounts to the indentation of the soft step calculated by the indentation model. Therefore, topography measurement of soft materials includes error due to sample indentation caused by repulsive forces.

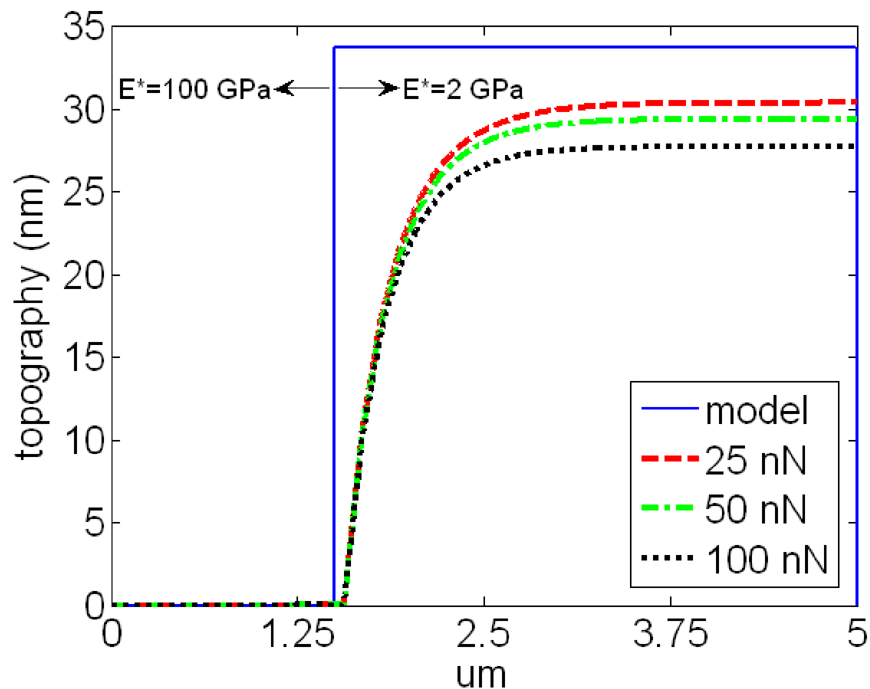

Figure 4.1 Simulated TRIF mode line scan of a soft step on a stiff surface. As the peak force is increased, the measured height of the step decreases due to indentation.

4.2 Verification of the Imaging Model

In order to test the validity of the imaging model, the results of imaging simulations by Legleiter [38] is referred to. In this work, the author investigates the effect of drive frequency and set point amplitude on interaction forces and topography measurement during tapping mode imaging. A cantilever probe is modeled to simulate the topography measurement of a 12 nm step with 2 GPa elastic modulus over a flat surface with an elastic modulus of 100 GPa. For a drive frequency at which the free cantilever oscillation amplitude is 90% of the free amplitude at resonance, the peak tapping forces vary from 6 nN to 13 nN on a 2 GPa surface when the set point ratio is varied from 0.9 to 0.5. For the same case of drive frequency and set point ratios, the simulated topography of the 2 GPa step ranges from 11.25 nm to 11.6 nm. In order to reproduce the results given above using our imaging model, the cantilever probe is modeled so that its response matches the one used by Legleiter [38]. The tip radius is chosen as 20 nm. Unlike TRIF mode where the probe is driven by the z-piezo, the cantilever is excited directly and the z-piezo only performs feedback, as the tapping mode configuration in figure 3.7 depicts. In figure 4.2, the blue line represents the sample topography described above with reduced elastic modulus values of 100 GPa and 2 GPa on low and high regions, respectively. The discontinuous lines show the simulated tapping mode topography measurements of this sample with the 90% drive frequency and set point amplitudes resulting in 9 nN, 11 nN, and 12 nN peak tapping forces. Simulated height values of the step are close to 11 nm which is slightly below the values in literature [21]. The small difference between the simulated topography values in figure 4.2 and the ones in literature may be due to the tip radius value used in simulations. According to equation 3.13, the indentation is inversely proportional to tip radius, implying that the tip radius value used by Legleiter may be larger than 20 nm. All in all, the simulations succeed in producing close enough results to published ones [21], which verify the imaging model.

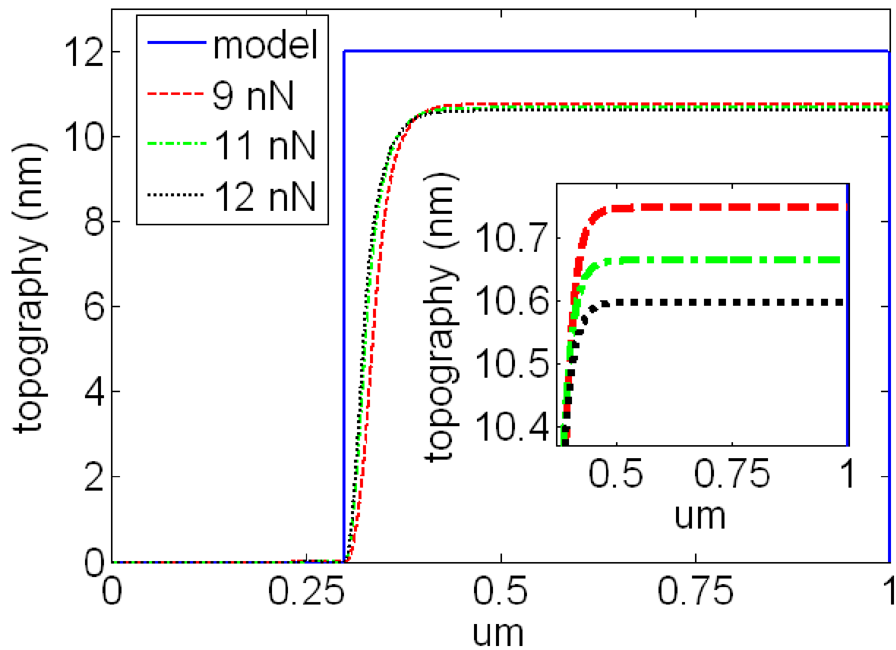

Figure 4.2 Simulated tapping mode line scan of a sample consisting of a 12 nm step with 2 GPa reduced elastic modulus over a flat surface with 100 GPa reduced elastic modulus. The simulated height of the step decreases as the peak tapping force increases. The height values agree well with simulation results in literature [21], which verifies the imaging model.

4.3 Effect of Adhesion Variations on Accurate Topography Measurement of Samples

In addition to elasticity variations, topography errors may result from adhesion variations. A step shaped topography with constant elasticity but varying adhesion is defined and this is shown in figure 4.3a. The adhesion hysteresis increases on the step, after the topography is completely tracked. First TRIF mode topography measurement simulation is performed with RMS control, where the RMS value of each tap is maintained at a desired value. As can be seen from figure 4.3b, after a certain point on the step, the adhesive force suddenly increases. This increases the RMS value of the interaction force signal. In order to preserve the desired RMS value of the taps, the controller decreases the peak force by adjusting the feedback signal, hence the z-piezo offset. The shift in the z-piezo position leads to topography measurement error, as the dashed red line indicates in figure 4.3a. This error can only be avoided by eliminating the

dependence of the control parameter on adhesive forces. Therefore, the same line scan simulation is performed with peak force control. In this case, variation of adhesive forces does not alter the peak force. Since the control parameter value remains constant, the feedback signal is unaltered, so is the measured topography. The simulated topography measurement is shown by the dash-dot green line in figure 6a. It is possible to eliminate topography errors due to adhesion variations, using peak force control. Yet, the error due to sample indentation is a consequence of large repulsive forces during imaging, and it cannot be eliminated by stand-alone peak force control. Minimum repulsive force is needed for minimizing the topography error.

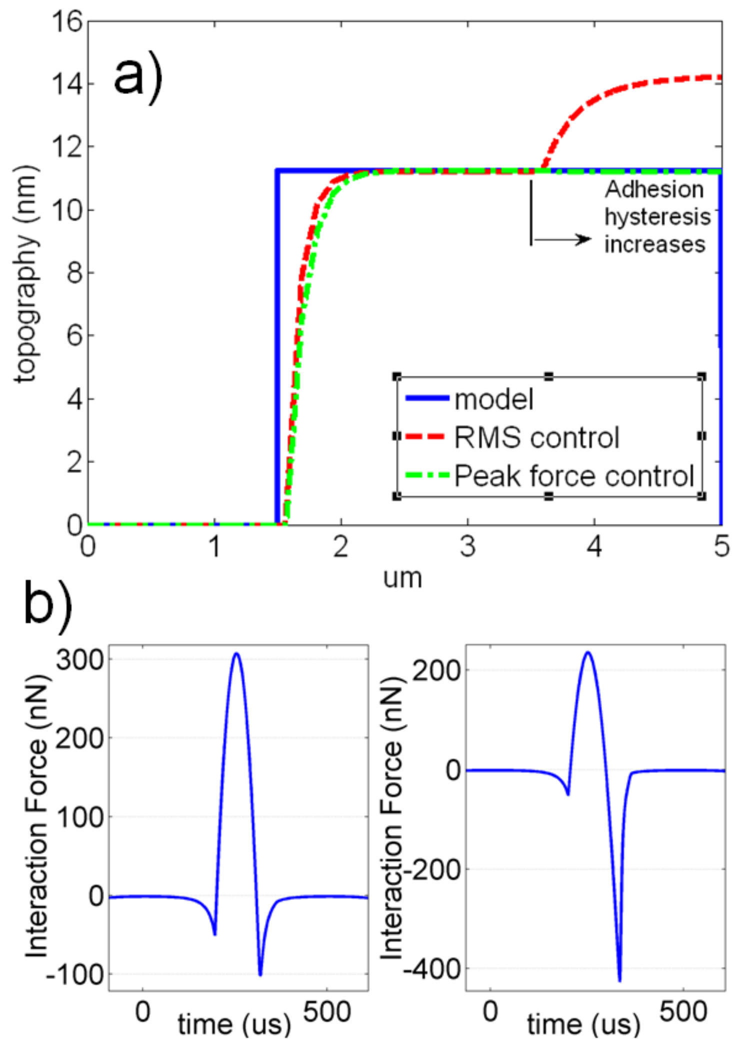

Figure 4.3 a) Simulated TRIF mode line scan of a step with constant elasticity but varying adhesion. Topography error due to adhesion can be eliminated by controlling the peak force value which is independent of adhesive forces. b) Interaction force signals during RMS control before (left), and after (right) the adhesion change.

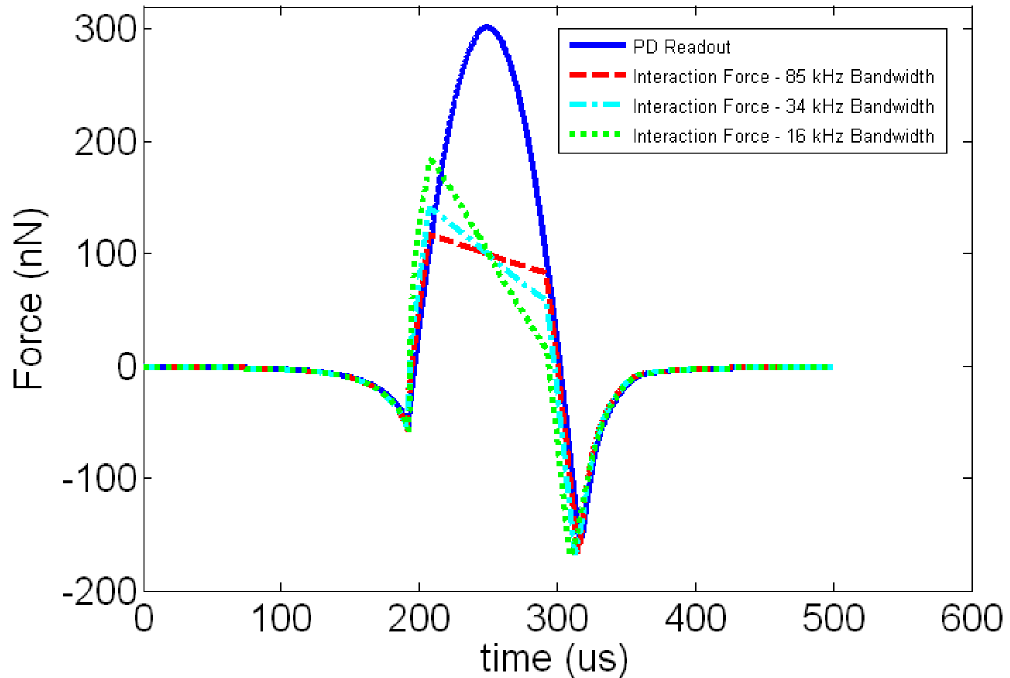

Figure 4.4 Response of FIRAT probes with different bandwidth values to ATC. FIRAT probes become more responsive to ATC when the probe bandwidth is larger.

4.4 Simulation of Passive and Active Tip Control Schemes

If active probes are employed in TRIF imaging, tip control is possible by using their integrated actuators. The responsiveness of FIRAT probe's electrostatic actuator to ATC can be tested using the imaging model. Ideally, the ATC voltage applied to the integrated actuators pulls back the beam during the contact to keep the contact force constant. However, this ideal response cannot be achieved since the FIRAT probes have finite bandwidth. ATC operation of FIRAT probes with different bandwidths is simulated and the results are shown in figure 4.4. In these simulations, ATC is activated when the repulsive force exceeds 100 nN. The solid blue line represents the photodiode readout while the rest of the curves represent the interaction force between the tip and the sample. The higher bandwidth device (85 kHz) responds fastest, therefore has a more flat response in the repulsive force region. As the bandwidth decreases (34 kHz, 16 kHz), the probe becomes less responsive to ATC. This results in higher repulsive force. As a result, high bandwidth is needed in order to effectively limit the repulsive forces using ATC.

One can also compare passive and active tip control schemes by simulation in order to discover their advantages and limitations. In passive control, the tip-sample forces are adjusted by moving the z-piezo, hence the probe base vertically. Direct actuation of the probe tip is not employed. Peak force control is analyzed as an example of passive control action. In figure 4.5a, simulated interaction force signals for different peak force values are shown. For a given desired peak force value, the feedback signal adjusts the piezo offset from the surface, effectively changing the tip sample force. In other words, while keeping the piezo movement amplitude constant, the offset from the surface is gradually increased to lower the peak force. Along with the peak force, contact time also decreases. In order to have stable contact with the sample, constant contact time is needed during force control. As seen in figure 4.5a, peak force control fails to provide stable contact for small peak forces, as the contact time gets shorter. Additionally, lack of sufficient contact time alters the characteristics of the interaction force curve that contain crucial material information such as the elastic modulus and the adhesion force. Even though the point of contact on the sample is the same, the slope of the repulsive force curve, which contains elastic modulus information, changes as the peak force is decreased. Similarly, the adhesion force on the tip is smaller for shorter contact time. Inconsistencies in the slope and salient features of the force curve increase the complexity of material characterization. ATC can overcome these shortcomings by providing constant contact time during force control. Figure 4.5b illustrates simulated interaction force signals during ATC. The solid blue curve is the photodiode readout, and the remaining curves represent the tip-sample force for different ATC force limits. Regardless of the force limit value, the contact time, hence stable contact is preserved. Additionally, since the slope and the salient features of the curves are unaltered as the force limit is decreased, more robust material characterization is possible. By means of ATC, the probe is stiff against attractive forces and soft against repulsive forces. This eliminates the stability-small force trade-off that regular cantilevers have.

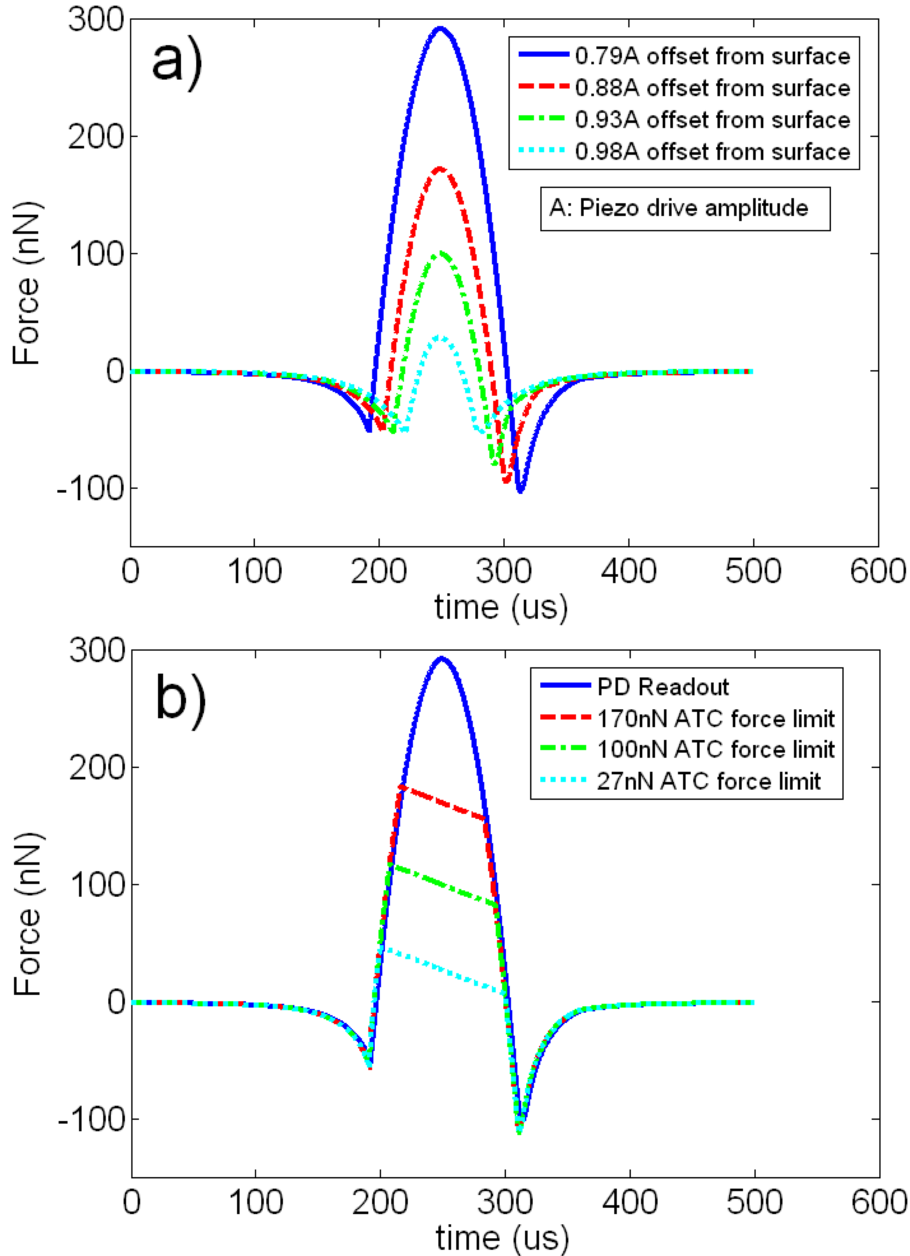

Figure 4.5 a) Contact time decreases for small repulsive forces during peak force control. The tip-sample contact becomes less stable and important material information such as elastic modulus and adhesion force is lost. b) Controlling repulsive forces with ATC provides sufficient contact time for stable contact and preserving material information.

4.4.1 Simulation of Topography Measurement by ATC

In this section, the effect of ATC on accurate topography measurement of samples with elasticity variations is investigated. The simulation results are compared with previously published experimental data [36]. Figures 4.6a and 4.6b show the test and the

control sample used in the experiments, respectively. The test sample is a soft polymer mixture (E = 2.8 GPa) patterned on silicon (E = 150 GPa). The control sample consists of chromium, silicon, and aluminum. The materials of interest in this sample are only the chromium (E = 279 GPa) and the silicon (E = 150 GPa). Both chromium and silicon are stiff materials.

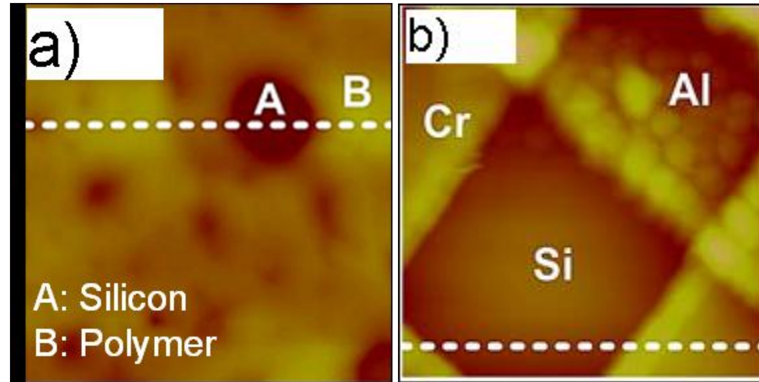

Figure 4.6 a) AFM image of the test sample composed of silicon (E=150GPa) and polymer (E=2.8GPa). b) AFM image of the control sample composed of chromium (E=279GPa) and silicon (150GPa) [36].

The test and control samples are defined in the simulation in a simpler manner. For both samples, a step shaped topography of arbitrary height is created, and the transition between materials occur on the higher region. The defined test and control samples and the respective simulated topography measurements with peak force control and ATC are given in figures 4.7a and 4.7b. The simulation parameters, including the FIRAT probe dimensions, user defined peak force and ATC force limit values, piezo movement amplitude and the like are matched with the experimental conditions [36]. As figure 4.7a depicts, when the transition from silicon to polymer occurs, larger indentation of polymer causes topography error. When the same line scan is simulated with ATC enabled, the repulsive forces are minimized; therefore the topography error is reduced by 2.26 nm. Figure 4.7b shows that the topography error improvement in the control sample by employing ATC is negligible (0.05 nm). The reason is both chromium and silicon are stiff materials and their indentation by the tip is already small.

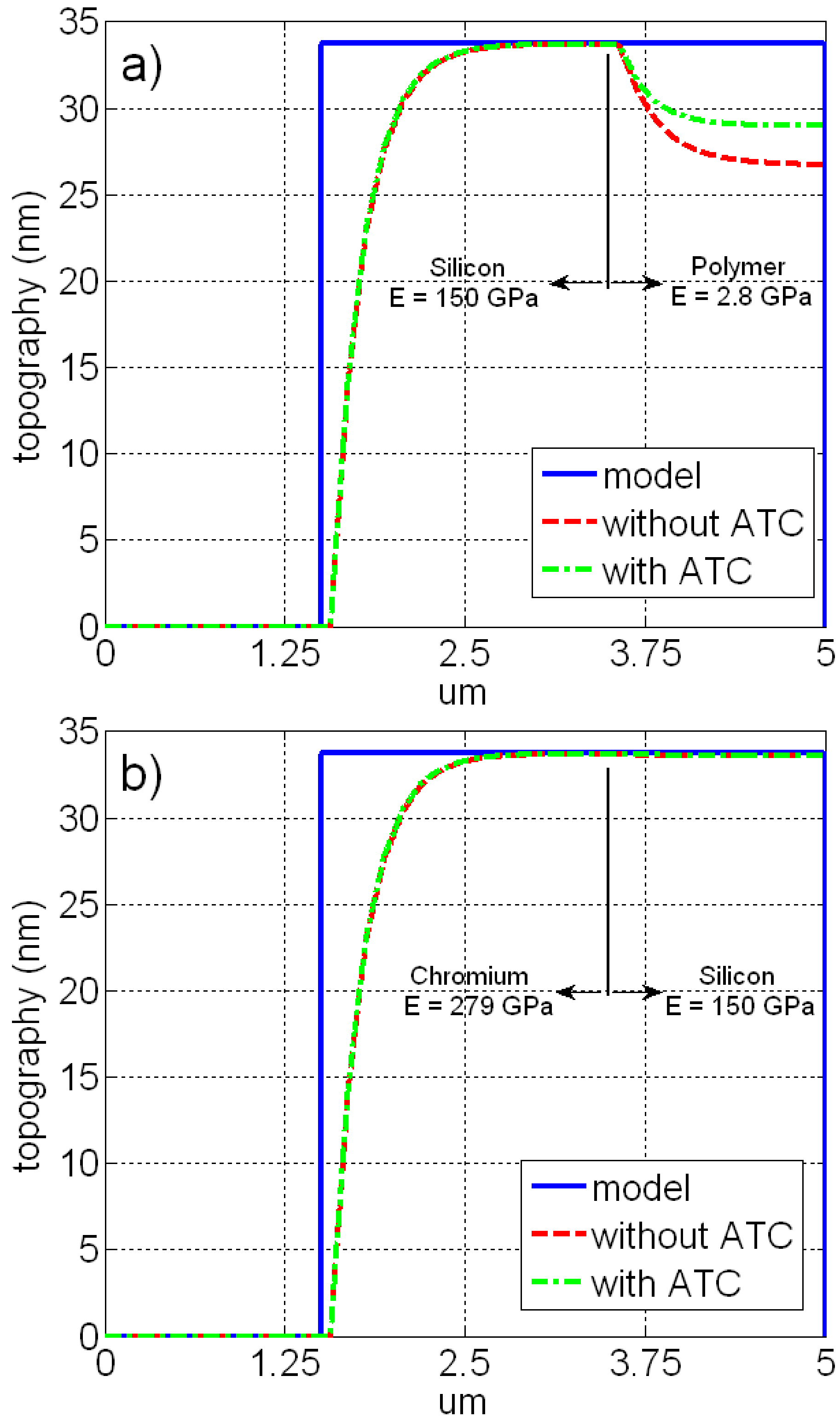

Figure 4.7 a) Simulated topography measurement of the test sample with and without ATC. ATC decreases the topography error of the polymer region by 2.26nm since repulsive forces on soft polymer are minimized. b) Simulated topography measurement of the control sample. The improvement is only 0.05nm since both chromium and silicon are stiff materials.

4.4.2 Experiment

The simulation results are confirmed by the published topography measurements of the same test and control samples [36]. In the test sample which is shown in figure 4.6a, the higher region is polymer and the lower region is silicon. The topography of a line similar to the one shown in figure 4.6a is measured with peak force control and ATC which are shown in figure 4.8a with dashed blue and solid red lines, respectively. In order to see the improvement by ATC, the difference between these two measurements is also plotted on the same figure with the dotted green line. Except for the spikes around the edges of topography, the difference is approximately 1 nm on the polymer region which is a result of minimizing sample indentation by ATC. In contrast, the indentation into the stiff silicon region is small, resulting in a difference of only 0.3 nm. In figure 4.8b, the same format is used for the control sample measurement curves. The measured topography of a line similar to the one shown in figure 4.6b is presented. Since both silicon and chromium are stiff materials, the improvement by employing ATC is around 0.1 nm. These results agree well with the simulation results for the fact that topography improvement values are in the same order of magnitude on specific materials for both test and control samples.

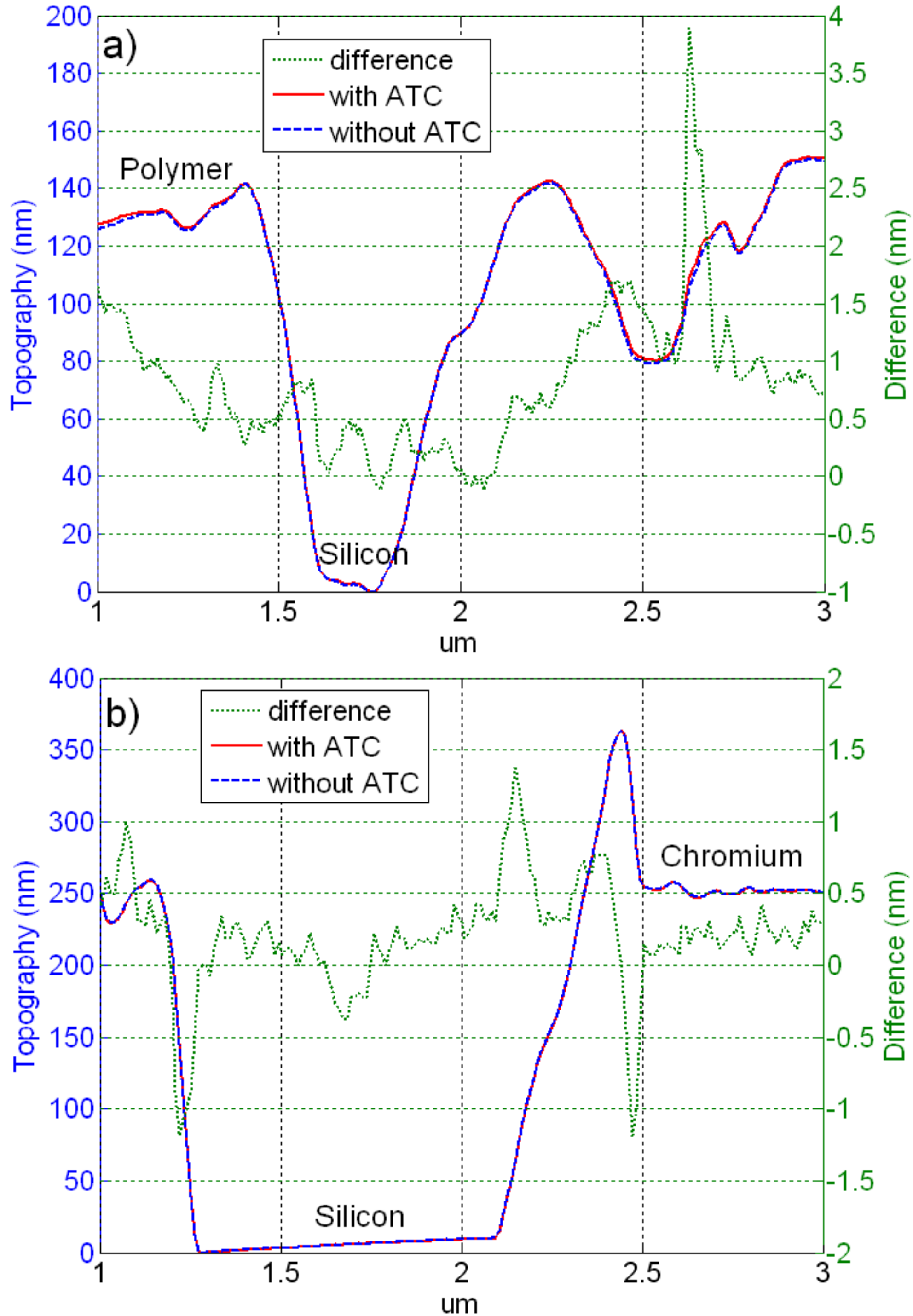

Figure 4.8 a) Measured topography of the test sample with (solid red line) and without (dashed blue line) ATC. The difference (dotted green line) between the two measurements is approximately 1nm on soft polymer, 0.3nm on stiff silicon, except for the spikes around the edges of topography. ATC improves topography measurement of the soft polymer region by minimizing the indentation. b) Measured topography of the control sample with (solid red line) and without (dashed blue line) ATC. The difference (dotted green line) is around 0.1nm on both silicon and chromium. Since the indentation into these stiff materials is already small, ATC improvement is negligible [36].

CHAPTER 5

CONCLUSION

The purpose of this research was to analyze TRIF mode AFM imaging in detail, using active and passive probes. For accomplishing this, a comprehensive AFM imaging model that is capable of simulating various imaging modes, probe structures, sample material properties, tip-sample interaction force models, and actuation and feedback schemes is developed. Using this model, the effect of variations in sample elasticity and adhesion on topography measurement is investigated for peak force and RMS control. Passive and active tip control schemes are simulated and examined in terms of stable contact and accurate material information. The effect of employing ATC on topography measurement during TRIF mode is also explored.

Simulation results demonstrate that topography errors may occur due to elasticity and adhesion variations when RMS control is used. Errors due to adhesion can be eliminated using peak force control, but elasticity based errors remain if passive cantilever probes are used. In order to minimize the topography errors due to indentation, minimal repulsive force and sample indentation is required. Decreasing repulsive forces is possible with passive cantilevers with peak force control, but this is achieved at the expense of stable contact and valuable material information such as elasticity and adhesion. ATC of FIRAT probe provides force control for minimizing sample indentation and topography errors while preserving sufficient contact time for stable contact and the information for material characterization. These results are supported by experiments performed with active FIRAT probes.

5.1 Future Work

The results presented in this thesis provide detailed analysis related to TRIF mode AFM imaging using active and passive probes. The model can be used to investigate

other imaging applications and material models. Additionally, more advanced imaging modes can be developed to investigate viscoelastic properties of materials. In this sense, the future work can be listed as, but is not limited to:

- ***Modeling combined ultrasonic and TRIF mode AFM imaging:*** In combined ultrasonic and TRIF mode, an active probe such as FIRAT probe is used. The probe is operated in TRIF mode for eliminating sample damage while the tip is actuated with a high frequency signal that provides more sensitive elasticity measurement on stiff samples. The imaging model in this thesis can be used to analyze this combined mode, with slight modifications to the model. These modifications would be updating the FIRAT probe model to include higher order modes of the probe and applying a high frequency signal input to the FIRAT probe model in TRIF mode simulations.
- ***Measuring viscoelastic properties of materials:*** Viscoelastic properties of materials are frequency dependent; therefore stand-alone TRIF mode cannot completely capture these properties. In combined ultrasonic and TRIF mode AFM, one can analyze the ultrasonic AFM output to image viscoelastic properties such as storage and loss moduli of the material. Note that TRIF signals are concurrently available for measuring the elastic modulus of compliant parts of the sample material. In addition, the comparison between the current elastic tip-sample interaction model and the measurements on viscoelastic samples would provide valuable information for developing more accurate interaction models that include viscoelasticity.
- ***Design changes in FIRAT Probe structure and actuation Scheme:*** The current generation of FIRAT probes has the flexible beam fabricated over a transparent substrate and diffraction gratings. As presented in this thesis, the probe base is excited vertically by an AFM z-piezo, which limits the actuation speed in TRIF mode. However, FIRAT probe's bandwidth is suitable for performing TRIF imaging at higher speeds. The FIRAT structure can be fabricated over a cantilever with diffraction gratings and this cantilever can be vertically actuated by a tapping piezo.

Therefore, TRIF mode imaging speed can be improved. Additionally, instead of a flexible beam, a FIRAT cantilever that has electrostatic actuation capability can be used as the force sensor.

- ***Simulating the effect of noise on elasticity measurements:*** The model presented in this thesis does not account for noise that is present during real life AFM experiments. Models of common noise sources such as laser intensity noise and thermal-mechanical noise can be added to simulated TRIF signals. The accuracy of elasticity inversion from these TRIF signals can be investigated.

APPENDIX A

ANALOG ATC CIRCUITRY FOR TRIF MODE AFM IMAGING

This appendix describes the ATC circuitry that can be used in TRIF Mode imaging experiments. The details of the related experimental setup are given in Chapter 3.

A.1 ATC Circuitry

The ATC circuitry used in TRIF mode AFM experiments mainly has two functions. One of them is to rectify the TRIF signal in order to generate the ATC signal. ATC circuitry is also equipped with a peak detector, which finds the peak value of TRIF signals at each interaction cycle. The schematic of the ATC circuitry is illustrated in figure A.1. It consists of five operational amplifiers (op-amp), and each individual op-amp is used to perform a specific function.

Op-amp 1 in figure A.1 is used to construct a non-inverting differential amplifier. The input to the non-inverting terminal is the TRIF signal whereas the input to the inverting terminal is the positive supply voltage. This aims to subtract a positive DC voltage from the TRIF voltage in order to adjust the user defined ATC threshold. The value of the DC voltage to be subtracted from the TRIF voltage is determined by the voltage divider consisting of a 5.1 kΩ resistor and 1 kΩ variable resistor. By changing the value of the variable resistor, the amount of DC voltage into the inverting terminal can be adjusted. Since all of the four resistors used in differential amplifier configuration are 10 kΩ, this circuit has unity gain. In short, the output of op-amp 1 is a negatively biased version of the input TRIF signal.

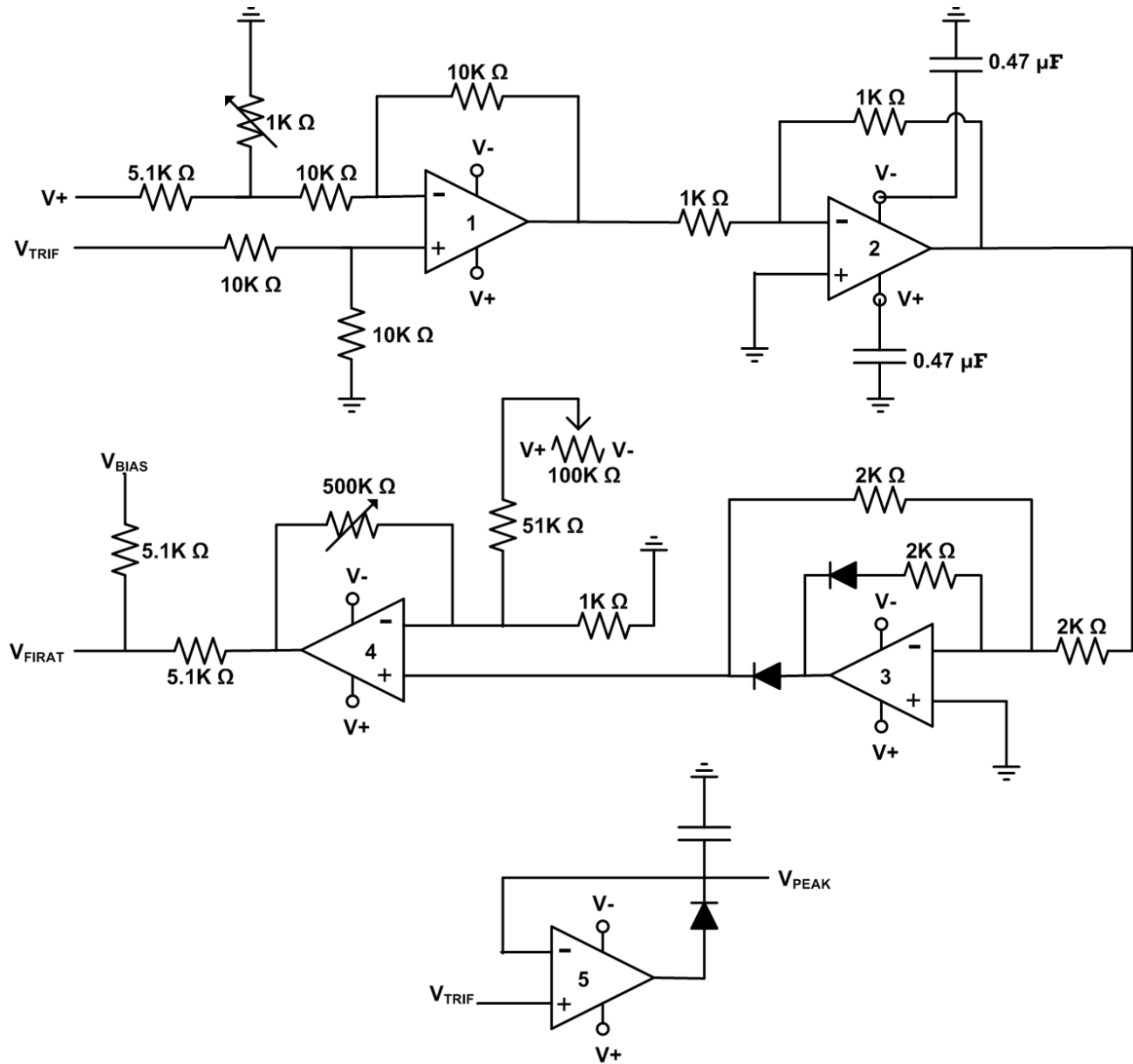

Figure A.1 The ATC circuitry used in TRIF Mode AFM imaging.

The circuit built with op-amp 2 is an inverting amplifier. This circuit also has a unity gain due to identical resistors, and the output is an inverted version of the input since the input voltage is applied to the inverting terminal of the op-amp. In addition to inverting the input signal, this circuit functions as a buffer to prevent any cross-talk between the circuit elements preceding and following the circuit. Therefore, the output of op-amp 1 is transferred to op-amp 3 without being distorted. The 0.47 µF capacitors that are connected between the supply voltage terminals of op-amp 2 and the ground reduce the unwanted oscillations in the output voltage.

Op-amp 3 in figure A.1 is utilized in a precision rectifier circuit. This circuit is a half wave rectifier which passes the positive portion of the signal, and blocks the negative portion. Note that this rectifier circuit is also in inverting configuration so that the signal inverted by the preceding circuit is inverted once more to reach its initial state. The resistor connected to the inverting terminal and the feedback resistors have identical resistance of 2 kΩ so that the circuit has no amplification factor. Note also that the diodes are connected to the op-amp output at opposite terminals. At this point of the ATC circuitry, the ATC signal is generated for a given TRIF signal and threshold value. However, the ATC signal needs to be amplified by an appropriate factor before being fed to the FIRAT probe electrostatically.

Op-amps internally generate a small offset voltage, which is visible in their output. This is problematic for the ATC operation since any undesired offset in the ATC signal would alter the electrostatic force applied to the probe tip. Fortunately, the cumulative offset that is present in the ATC signal can be eliminated by using an offset trimmer circuit. Op-amp 4 in figure A.1 is used to construct an offset trimmer with adjustable gain. The ATC signal is fed to the non-inverting terminal of op-amp 4 and a small corrective offset is applied to the inverting terminal. The variable 100 kΩ resistor is used to adjust the amplitude of this corrective offset signal. Moreover, the 1 kΩ and variable 500 kΩ resistors form a non-inverting amplifier configuration. The variable resistor is used to determine the factor by which the ATC signal is amplified. Eventually, the desired ATC signal is available at the output terminal of op-amp 4. As discussed in Chapter 2, a bias voltage is applied to the FIRAT probe for optimal measurement sensitivity. Hence, this bias voltage needs to be combined with the ATC signal before FIRAT probe is actuated. The 5.1 kΩ resistor pair forms a summing junction that combine these two signals and yield the overall actuation signal. Note that this summation decreases the amplitude of both the bias and the ATC signals to half of the

original amplitudes. Therefore, the bias voltage and the ATC amplification factor should be chosen accordingly.

The circuitry given in figure A.1 also contains a simple peak detection circuit that can detect the peak value of the TRIF signal. This circuit is built using op-amp 5. A diode is connected to the op-amp in negative feedback configuration while a capacitor is placed between the ground and the diode output. The TRIF signal is fed to the non-inverting terminal of the op-amp and the peak value of this signal is obtained from the diode output. The peak voltage remains constant until the upcoming peak is detected. The peak voltage is fed to a PID controller in order to perform feedback control based on the peak value of the interaction forces.

APPENDIX B

FPGA IMPLEMENTATION OF ATC AND PEAK FORCE BASED PID CONTROL

This appendix explains the FPGA program that can be used to perform operations such as ATC, peak detection, and PID control.

B.1 FPGA Program

Analog circuits can be preferred to perform operations such as feedback control for their fast response. However, they cannot be very easily configured to adjust parameters such as controller gains since this requires replacing resistors or capacitors. In this sense, field programmable gate array (FPGA) circuits provide more flexibility in terms of changing operation parameters or including additional functionality. An FPGA is a programmable digital logic circuit that can be configured according to user determined algorithms. Low level programming languages such as VHDL or Verilog can be used to program FPGAs. However, Labview FPGA Module® provides a graphical user interface to program FPGAs which is a more convenient option.

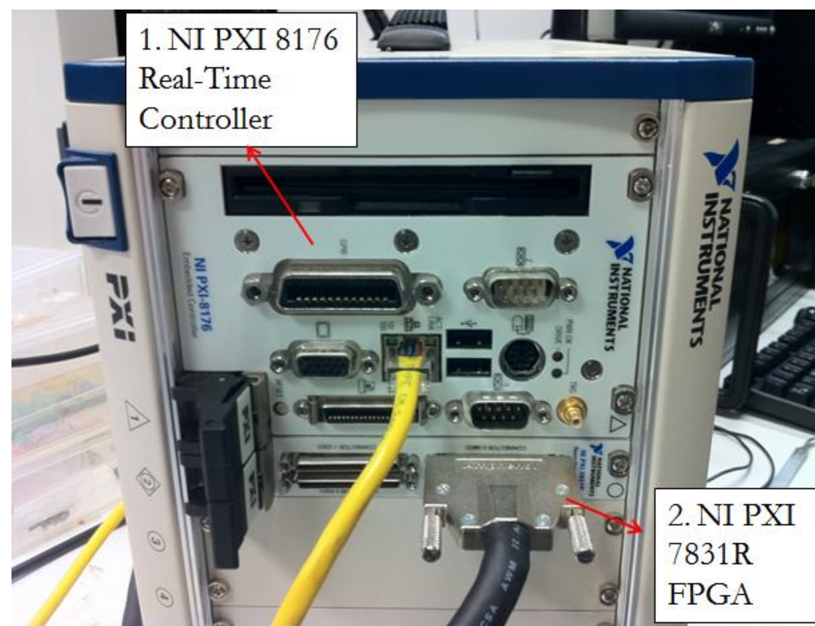

Figure B.1 NI PXI 8176 real-time controller and NI PXI 7831R FPGA.

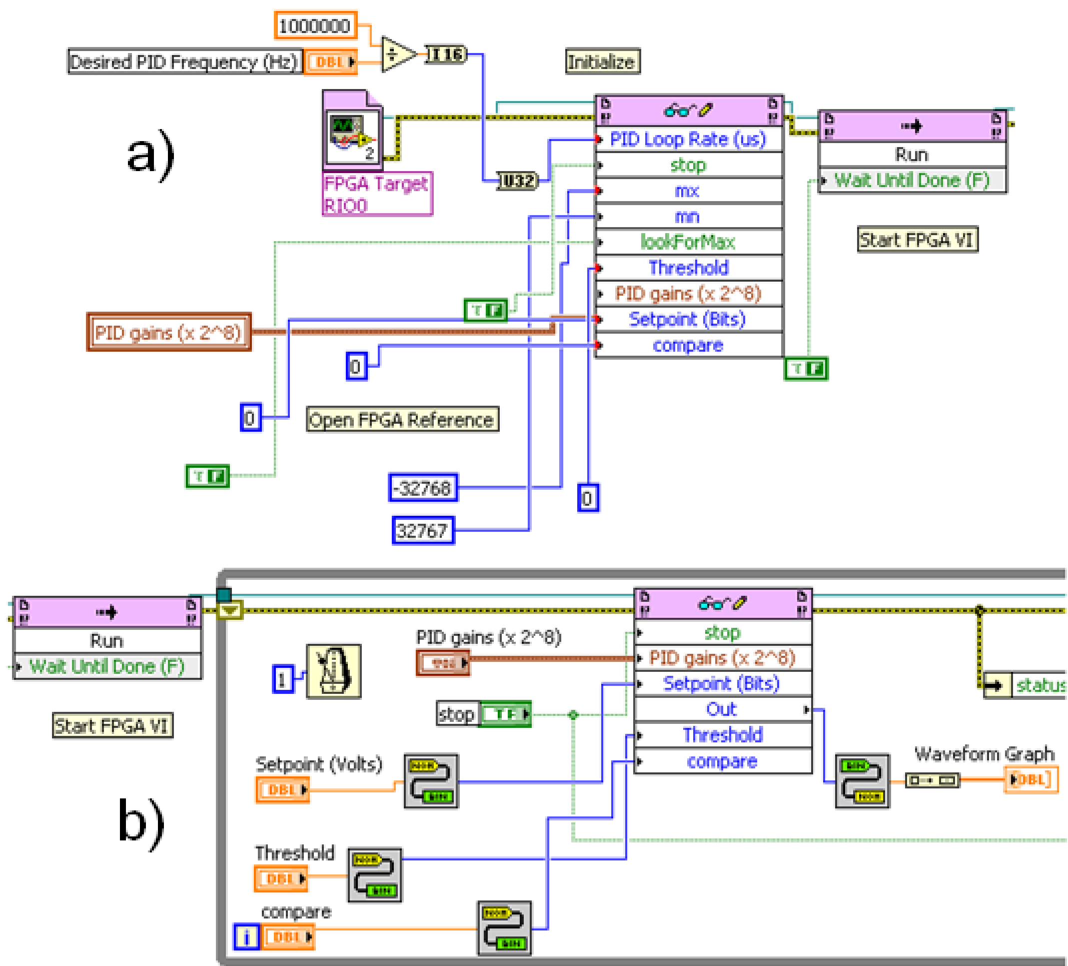

Figure B.2 Real-time controller program. Bottom portion (b) is the continuation of the top portion (a).

Figure B.1 shows an NI PXI 8176 real-time controller combined with an NI PXI 7831R FPGA. This hardware is programmed so that a peak force based PID algorithm can be performed. The real-time controller is used to perform operations such as receiving input parameters, and transferring these variables to the FPGA. On the other hand, the FPGA is used to implement the desired algorithm. Figure B.2 depicts the real-time controller program prepared in Labview. This program receives the desired PID rate, PID gains, the set point peak force value, and FPGA output voltage limits (figure B.2a). In a while loop (figure B.2b), these parameters are continuously transferred to the FPGA program. Additionally, functions such as starting and stopping the FPGA program are performed using the real-time controller program.

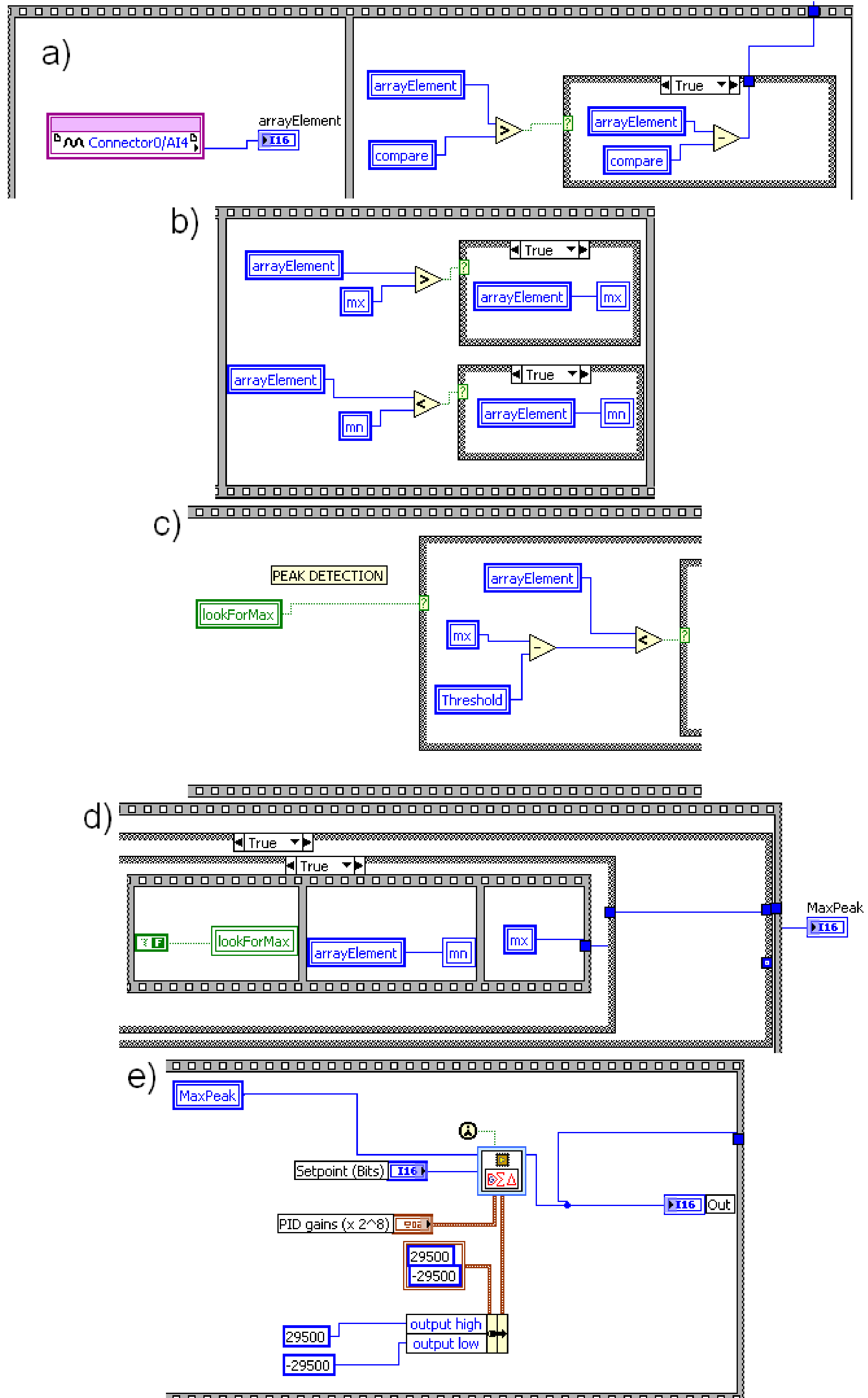

Figure B.3 Sections of the FPGA program for ATC (a), peak detection (b, c, d) and PID control (e).

Figure B.3 shows the FPGA program as divided into consecutive sections. Each of these sections has frames that divide the program into smaller portions. These frames force the FPGA to execute these small portions of code in the given sequence. The FPGA is equipped with an analog-to-digital (ADC) converter which digitizes the input TRIF signal. Therefore, the FPGA program receives and processes a single data point in each cycle of the loop. As given in figure B.3a, the input data point is transferred from an input block to the variable 'arrayElement'. This data point is compared with the ATC threshold which is represented by the variable 'compare'. If the given data point is larger than the threshold, the difference between them is sent to the digital-to-analog (DAC) converter to be generated as the ATC output.

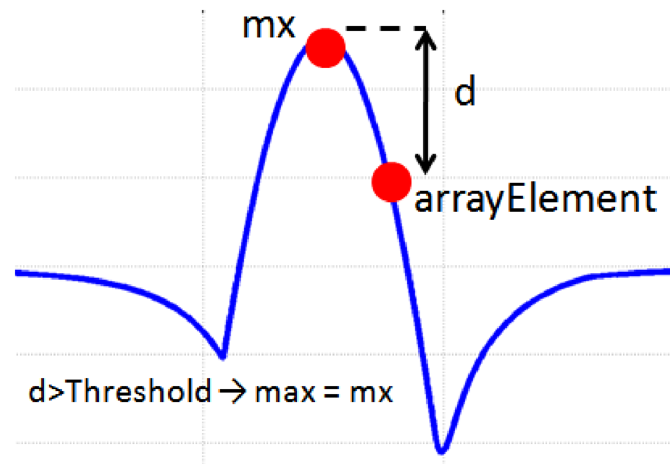

Figure B.4 Graphical illustration of the peak detection algorithm.

In figures B.3b, B.3c, B.3d, the peak detection portion of the FPGA program is illustrated. There are two key variables in this peak detection algorithm. These variables are 'mx' and 'mn'. Initially, mx and mn are set to '-Infinity' and '+Infinity', respectively. Therefore, when compared with the arrayElement for the first time, the value of both mx and mn is arrayElement (figure B.3b). As new data points are introduced, the values of mx and mn are updated. For instance, if the new arrayElement value is greater than the current mx value, arrayElement is assigned to mx (figure B.3b). The variables mx and mn are candidates for the detected maximum and the minimum value of the TRIF signal,

respectively. Note that only the maximum value detection will be discussed here, but the minimum detection is the identical process. The variable ‘lookForMax’ (figure B.3c) is a Boolean that determines whether the maximum or the minimum value is being explored. Another important variable, ‘Threshold’ (figure B.3c) determines the desired value of difference between a detected maximum candidate and the current data point. This can be more clearly explained referring to the illustration in figure B.4. Figure B.4 graphically illustrates the process in figures B.3c and B.3d. If the difference, d between the current values of arrayElement and mx is greater than the user defined value of Threshold (figure B.3c), then the current value of mx becomes the detected maximum value of the input signal (figure B.3d). The value of Threshold enables one to avoid local maxima or minima. As Threshold becomes smaller, peaks with smaller amplitude can be detected. By the choice of a reasonable Threshold value, one can eliminate detecting undesired noise peaks. Once the maximum is detected, the value of arrayElement is assigned to mn, and the value of lookForMax is changed to false (figure B.3d) so that the program begins to explore the minimum value of the input signal.

Figure B.3e depicts the portion of the FPGA program that performs PID control. In this portion of the program, Labview’s built-in PID control block is used. For a detected peak force value and user defined values of set point peak force, PID gains, and output voltage limits, the PID block computes the control signal that is fed to the AFM z-piezo. At this point, the FPGA loop is completed.

B.2 Comments

Utilizing an FPGA for TRIF Mode AFM experiments is a convenient choice for the fact that FPGAs can be easily configured to change operation parameters and to implement additional tasks. However, for the particular FPGA system discussed here, the digitization rate is a limitation. NI PXI 7831R has an ADC converter that has a maximum sampling rate of 200 kS/s [52]. For the program described above, the effective loop rate

of this FPGA is measured to be 166 kHz. Although this speed is sufficient for controlling the z-piezo at 2 kHz in TRIF Mode, performing ATC requires much larger rates. ATC requires virtually no delay between the TRIF signal and the generated ATC signal so that the tip can be correctly controlled. This is why the analog ATC circuitry given in Appendix A should be preferred. Although analog circuits are favored for their speed, an FPGA with a fast enough digitizer would be ideal for building an easily configurable experimental setup for imaging with FIRAT probe.

REFERENCES

[1] G. Binnig, C. F. Quate, and C. Gerber, "Atomic Force Microscope," *Physical Review Letters,* vol. 56, pp. 930-933, 1986.

[2] P. M. Bridger, Z. Z. Bandic, E. C. Piquette, and T. C. McGill, "Measurement of Induced Surface Charges, Contact Potentials, and Surface States in GaN by Electric Force Microscopy," *Applied Physics Letters,* vol. 74, pp. 3522-3524, 1999.

[3] A. Noy, C. D. Frisbie, L. F. Rozsnyai, M. S. Wrighton, and C. M. Lieber, "Chemical Force Microscopy: Exploiting Chemically-Modified Tips To Quantify Adhesion, Friction, and Functional Group Distributions in Molecular Assemblies," *Journal of the American Chemical Society,* vol. 117, pp. 7943-7951, 1997.

[4] F. J. Giessibl, S. Hembacher, H. Bielefeldt, and J. Mannhart, "Subatomic Features on the Silicon (111)-(7x7) Surface Observed by Atomic Force Microscopy," *Science,* vol. 289, pp. 422-425, 2000.

[5] S. Alexander, L. Hellemans, O. Marti, J. Schneir, V. Elings, P. K. Hansma, M. Longmire, and J. Gurley, "An Atomic Resolution Atomic Force Microscope Implemented Using an Optical Lever," *Journal of Applied Physics,* vol. 65, pp. 164-167, 1989.

[6] Q. Zhong, D. Inniss, K. Kjoller, and V. B. Ellings, "Fractured polymer/silica fiber surface studied by tapping mode atomic force microscopy," *Surface Science,* vol. 290, pp. 688-692, 1993.

[7] S. N. Magonov, V. Elings, and M.-H. Whangbo, "Phase imaging and stiffness in tapping mode atomic force microscopy," *Surface Science,* vol. 375, pp. 385-391, 1997.

[8] O. Sahin and A. Atalar, "Simulation of higher harmonics generation in tapping-mode atomic force microscopy," *Applied Physics Letters,* vol. 79, pp. 4455-4457, 2001.

[9] T. R. Rodriguez and R. Garcia, "Tip motion in amplitude modulation (tapping-mode) atomic-force microscopy: Comparison between continuous and point-mass models," *Applied Physics Letters,* vol. 80, pp. 1646-1648, 2002.

[10] M. Stark, R. W. Stark, W. M. Heckl, and R. Guckenberger, "Inverting dynamic force microscopy: From signals to time-resolved interaction forces," *Proceedings of the National Academy of Sciences of the United States of America,* vol. 99, pp. 8473-8478, 2002.

[11] A. L. Weisenhorn, P. K. Hansma, T. R. Albrecht, and C. F. Quate, "Forces in atomic force microscopy in air and water," *Applied Physics Letters,* vol. 54, pp. 2651-2653, 1989.

[12] M. Radmacher, J. P. Cleveland, M. Fritz, H. G. Hansma, and P. K. Hansma, "Mapping Interaction Forces with the Atomic Force Microscope," *Biophysical Journal,* vol. 66, pp. 2159-2165, 1994.

[13] K. O. van der Werf, C. A. J. Putman, B. G. de Grooth, and J. Greve "Adhesion force imaging in air and liquid by adhesion atomic force microscopy," *Applied Physics Letters,* vol. 65, pp. 1195-1197, 1994.

[14] P. J. de Pablo, J. Colchero, J. Gomez-Herrero, and A. M. Baro, "Jumping mode scanning force microscopy," *Applied Physics Letters,* vol. 73, pp. 3300-3302, 1998.

[15] A. Rosa-Zeiser, E Weilandt, S. Hild, and O. Marti, "The simultaneous measurement of elastic, electrostatic and adhesive properties by scanning force microscopy: pulsed-force mode operation," *Measurement Science and Technology,* vol. 8, pp. 1333-1338, 1997.

[16] A. Gigler, C. Gnahm, O. Marti, T. Schimmel, and S. Walheim, "Towards quantitative materials characterization with Digital Pulsed Force Mode imaging," *Journal of Physics: Conference Series,* vol. 61, pp. 346-351, 2007.

[17] O. Marti, M. Holzwarth, and M. Beil, "Measuring the nanomechanical properties of cancer cells by digital pulsed force mode imaging," *Nanotechnology,* vol. 19, p. 384015, 2008.

[18] http://www.veeco.com/pdfs/appnotes/quantitative-mechanical-property-mapping-at-the-nanoscale-with-peakforce-qnm-an128-lores.pdf

[19] P. Maivald, H. J. Butt, S. A. C. Gould, C. B. Prater, B. Drake, J. A. Gurley, V. B. Elings, and P. K. Hansma , "Using force modulation to image surface elasticities with the atomic force microscope," *Nanotechnology,* vol. 2, pp. 103-106, 1991.

[20] H.-U. Krotil, Th. Stifter, and O. Marti, "Concurrent measurement of adhesive and elastic surface properties with a new modulation technique for scanning force microscopy," *Rev. Sci. Instrum,* vol. 71, pp. 2765-71, 2000.

[21] M. Balantekin and A. Atalar, "Enhancing higher harmonics of a tapping cantilever by excitation at a submultiple of its resonance frequency," *Physical Review B,* vol. 71, p. 125416, 2005.

[22] M. Balantekin and A. Atalar, "Enhanced higher-harmonic imaging in tapping-mode atomic force microscopy," *Applied Physics Letters,* vol. 87, p. 243513, 2005.

[23] O. Sahin, G. Yaralioglu, R. Grow, S. F. Zappe, A. Atalar, C. Quate and O. Solgaard, "High-resolution imaging of elastic properties using harmonic cantilevers," *Sensors and Actuators,* vol. 114, pp. 183-190, 2004.

[24] O. Sahin, S. Magonov, C. Su, C. F. Quate, and O. Solgaard, "An atomic force microscope tip designed to measure time-varying nanomechanical forces," *Nature Nanotechnology,* vol. 2, pp. 507-514, 2007.

[25] G. G. Yaralioglu, A. Atalar, S. R. Manalis, and C. F. Quate, "Analysis and design of an interdigital cantilever as a displacement sensor," *Journal of Applied Physics,* vol. 83, pp. 7405-7415, 1998.

[26] A. F. Sarioglu and O. Solgaard, "Cantilevers with integrated sensor for time-resolved force measurement in tapping-mode atomic force microscopy," *Applied Physics Letters,* vol. 93, p. 023114, 2008.

[27] D. C. Hurley, M. Kopycinska-Muller, A. B. Kos, and R. H. Geiss, "Nanoscale elastic-property measurements and mapping using atomic force acoustic microscopy method," *Measurement Science and Technology,* vol. 16, pp. 2167-2172, 2005.

[28] Z. Parlak and F. L. Degertekin, "Contact stiffness of finite size subsurface defects for atomic force microscopy: Three-dimensional finite element modeling and experimental verification," *Journal of Applied Physics,* vol. 103, p. 114910, 2008.

[29] O. Sahin and N. Erina, "High-resolution and large dynamic range nanomechanical mapping in tapping-mode atomic force microscopy," *Nanotechnology,* vol. 19, p. 445717, 2008.

[30] F. J. Giessibl, "Advances in atomic force microscopy," *Reviews of Modern Physics,* vol. 75, p. 949, 2003.

[31] C. Su, L. Huang, and K. Kjoller, "Direct measurement of tapping force with a cantilever deflection force sensor," *Ultramicroscopy,* vol. 100, pp. 233-239, 2004.

[32] A. G. Onaran, M. Balantekin, W. Lee, W. L. Hughes, B. A. Buchine, R. O. Guldiken, Z. Parlak, C. F. Quate, and F. L. Degertekin, "A new atomic force microscope probe with force sensing integrated readout and active tip," *Review of Scientific Instruments,* vol. 77, p. 023501, 2006.

[33] W. Lee, N. A. Hall, Z. Zhou, and F. Levent Degertekin, "Fabrication and Characterization of a Micromachined Acoustic Sensor With Integrated Optical Readout," *IEEE Journal of Selected Topics in Quantum Electronics,* vol. 10, pp. 643-651, 2004.

[34] F. L. Degertekin, A. G. Onaran, M. Balantekin, and W. Lee, "Sensor for direct measurement of interaction forces in probe microscopy," *Applied Physics Letters,* vol. 87, p. 213109, 2005.

[35] M. Balantekin, A. G. Onaran, and F. L. Degertekin, "Quantitative mechanical characterization of materials at the nanoscale through direct measurement of time-resolved tip–sample interaction forces," *Nanotechnology,* vol. 19, p. 085704, 2008.

[36] Z. Parlak, R. Hadizadeh, M. Balantekin, and F. L. Degertekin, "Controlling tip-sample interaction forces during a single tap for improved topography and mechanical property imaging of soft materials by AFM," *Ultramicroscopy,* vol. 109, pp. 1121-1125, 2009.

[37] Z. Parlak and F. L. Degertekin, "Combined quantitative ultrasonic and time-resolved interaction force AFM imaging," *Review of Scientific Instruments,* vol. 82, p. 013703, 2011.

[38] J. Legleiter, "The effect of drive frequency and set point amplitude on tapping forces in atomic force microscopy: simulation and experiment," *Nanotechnology,* vol. 20, p. 245703, 2009.

[39] S. C. Minne, S. R. Manalis, and C. F. Quate,"Parallel atomic force microscopy using cantilevers with integrated piezoresistive sensors and integrated piezoelectric actuators," *Applied Physics Letters,* vol. 67, pp. 3918-3920, 1995.

[40] B. Rogers, T. Sulchek, K. Murray, D. York, M. Jones, L. Manning, S. Malekos, B. Beneschott, J. D. Adams, H. Cavazos, and S. C. Minne, "High speed tapping mode atomic force microscopy in liquid using an insulated piezoelectric cantilever," *Review of Scientific Instruments,* vol. 74, pp. 4683-4686, 2003.

[41] S. D. Senturia, *Microsystem design*. Boston :: Kluwer Academic Publishers, 2001.

[42] B. Bhushan, *Handbook of Micro/Nano tribology / Second Edition Edited by Bharat Bhushan.* Boca Raton: CRC Press, 1999.

[43] B. Kumar, P. M. Pifer, A. Giovengo, and J. Legleiter, "The effect of set point ratio and surface Young's modulus on maximum tapping forces in fluid tapping mode atomic force microscopy," *Journal of Applied Physics,* vol. 107, p. 044508, 2010.

[44] G. Schitter, P. Menold, H. F. Knapp, F. Allgower, and A. Stemmer, "High performance feedback for fast scanning atomic force microscopes," *Review of Scientific Instruments,* vol. 72, pp. 3320-3327, 2001.

[45] G. Schitter, F. Allgower, and A. Stemmer, "A new control strategy for high-speed atomic force microscopy," *Nanotechnology,* vol. 15, pp. 108-114, 2004.

[46] N. A. Hall and F. L. Degertekin, "Integrated optical interferometric detection method for micromachined capacitive acoustic transducers," *Applied Physics Letters,* vol. 80, pp. 3859-3861, 2002.

[47] T. Sulchek, R. Hsieh, J. D. Adams, G. G. Yaralioglu, S. C. Minne, C. F. Quate, J. P. Cleveland, A. Atalar, and D. M. Adderton, "High-speed tapping mode imaging with active Q control for atomic force microscopy," *Applied Physics Letters,* vol. 76, pp. 1473-1475, 2000.

[48] T. Sulchek, G. G. Yaralioglu, C. F. Quate, and S. C. Minne, "Characterization and optimization of scan speed for tapping-mode atomic force microscopy," *Review of Scientific Instruments,* vol. 73, pp. 2928-2936, 2002.

[49] T. Ando, T. Uchihashi, N. Kodera, D. Yamamoto, A. Miyagi, M. Taniguchi, and H. Yamashita, "High-speed AFM and nano-visualization of biomolecular processes," *Pflugers Arch - Eur J Physiol,* vol. 456, pp. 211–225, 2007.

[50] U. Rabe, S. Amelio, E. Kester, V. Scherer, S. Hirsekorn, and W. Arnold, "Quantitative determination of contact stiffness using atomic force acoustic microscopy," *Ultrasonics,* vol. 38, pp. 430-437, 2000.

[51] F. L. Degertekin, "Integrated displacement sensors for probe microscopy and force spectroscopy," U.S. Patent Application 20070103697A1, May 10, 2007.

[52] http://sine.ni.com/nips/cds/view/p/lang/en/nid/11873